Computers and Geotechnics 184 (2025) 107286

Contents lists available at ScienceDirect

Computers and Geotechnics

journal homepage: www.elsevier.com/locate/compgeo

Research Paper

Mineral grain-texture model and impact on microcracking and mechanical response of granite

Suifeng Wang [a], Tao Wang [a], Derek Elsworth [b], Xianyu Zhao [c], Liping Zhang [a,*]

[a] State Key Laboratory of Water Resources Engineering and Management, Wuhan University, Wuhan, China
[b] Department of Energy and Mineral Engineering, EMS Energy Institute and G3 Center, Pennsylvania State University, University Park, PA, USA
[c] College of Hydraulic and Environmental Engineering, China Three Gorges University, Yichang, China

ARTICLE INFO

Keywords:
Mineral Grain
Heterogeneity
Anisotropy
Grain-texture model
Crystalline rock

ABSTRACT

Granites are representative of generic crystalline rocks characterized by their complex crystal-grain structure. Variations in the composition, size, shape and orientation of mineral grains result in pronounced heterogeneity and anisotropy at the microscopic scale, significantly influencing mechanical properties as well as the initiation and propagation of microcracks. A grain-texture model (GTM) is used to characterize the microstructural features of porphyritic monzogranite, based on the "templated" – "grain growth" method. This addresses the limitations inherent in Grain-Based Models (GBM) that do not allow for modifications to mineral grain shapes. The accuracy of this novel model was validated through comparisons between numerical and experimental results. Subsequent validations were against granite models with varying biotite contents to examine related mechanical and microcracking response as a result of component mineral properties, shape and orientation. Changes in biotite content influence heterogeneity and consequently both mechanical properties and failure characteristics of the composite granites. As biotite strength decreases, there is an increased likelihood for cracks to initiate and propagate within it; correspondingly, the decrease in stiffness of the biotite has a notable impact on the pattern and path of crack propagation. Alteration in the shape and orientation of mineral grains results in significant changes in the anisotropy of granite through impact on the number and arrangement of grain boundary contacts. When these boundary contact orientations align with fracture directions, rocks exhibit an increased propensity for the evolution of throughgoing fractures and macroscale failure.

1. Introduction

Granites possess remarkable physical and mechanical characteristics as strong and hard rocks, resistant to weathering and corrosion and comprising crucial components of many deep-seated hot-dry rock geothermal reservoirs (Zhuang and Zang, 2021; Kumari and Ranjith, 2019). Typical components are of quartz, feldspar, and biotite and with a complex crystal structure (Zhuang et al., 2019; 2020; Wang et al., 2024a; Zhang et al., 2024). Variations in mineral grain composition, size, shape and orientation result in significant heterogeneity and anisotropy at the microscopic scale. These characteristics influence its mechanical properties as well as the initiation and propagation of microcracks (Zhao et al., 2021; Li et al., 2022; Wang et al., 2025; Kong et al., 2024).

The presence of biotite exerts a considerable influence on the mechanical properties and failure characteristics of granites due to their relatively low strength and stiffness (Zhou et al., 2024; Geng et al., 2024; Mahabadi et al., 2014). Compression and hydraulic fracturing tests conducted on granites by Zhou et al. (2024) and Zhuang et al. (2020) showed that microcracks typically initiated and propagated along grain boundaries (GBs) with biotite minerals. Biotite can accumulate substantial reserves of strain energy through deformation, thereby influencing subsequent crack propagation. Mineral grain shape and orientation impact the mechanical properties and failure characteristics of granite (Ghazvinian et al., 2014), revealing that the anisotropy of mineral grains significantly modifies the macroscopic strength and elastic modulus of granite samples. These findings demonstrate that both biotite minerals and their shape and orientation substantially affect mechanical performance and crack propagation in crystalline rocks. However, due to the poorly defined and complex impacts of mineral composition, shape, orientation and structure on mechanical response – the quantitative impacts on granite aggregates containing biotite remain

* Corresponding author.
E-mail address: zhanglp@whu.edu.cn (L. Zhang).

https://doi.org/10.1016/j.compgeo.2025.107286
Received 21 December 2024; Received in revised form 30 March 2025; Accepted 14 April 2025
Available online 19 April 2025

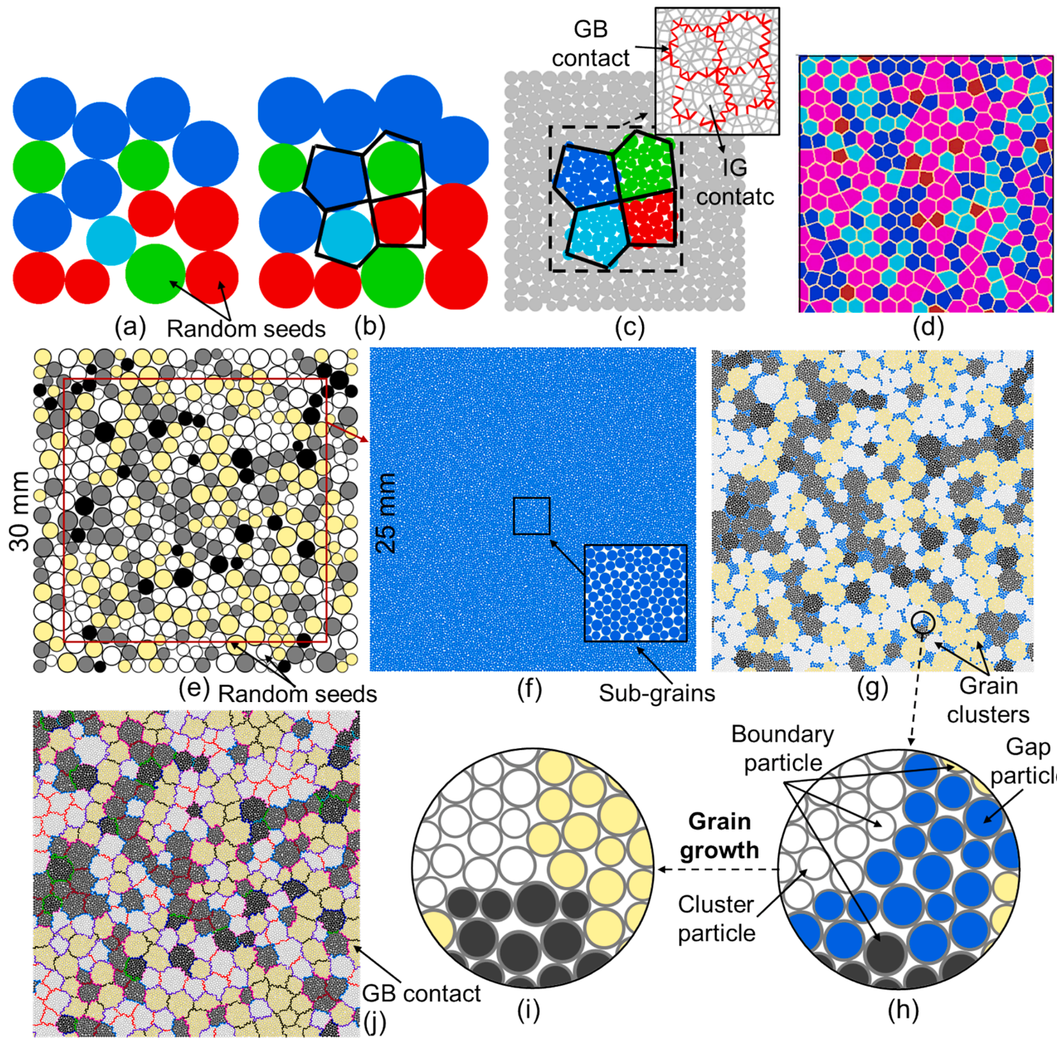

Fig. 1. Modeling process of GBM and GTM: (a) – (c): GBM method based on random grain seeds; (d) GBM (Liu et al., 2019); (e) – (j): GTM method based on the "templated" – "grain growth" method.

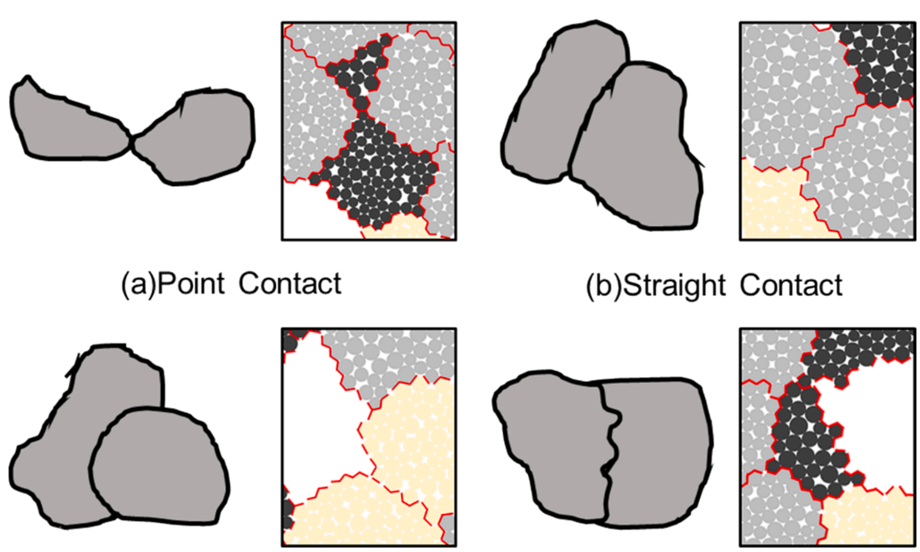

Fig. 2. The GTM model successfully reproduces the four mineral grain contact patterns in igneous rocks summarized by Ulusay et al. (1994).

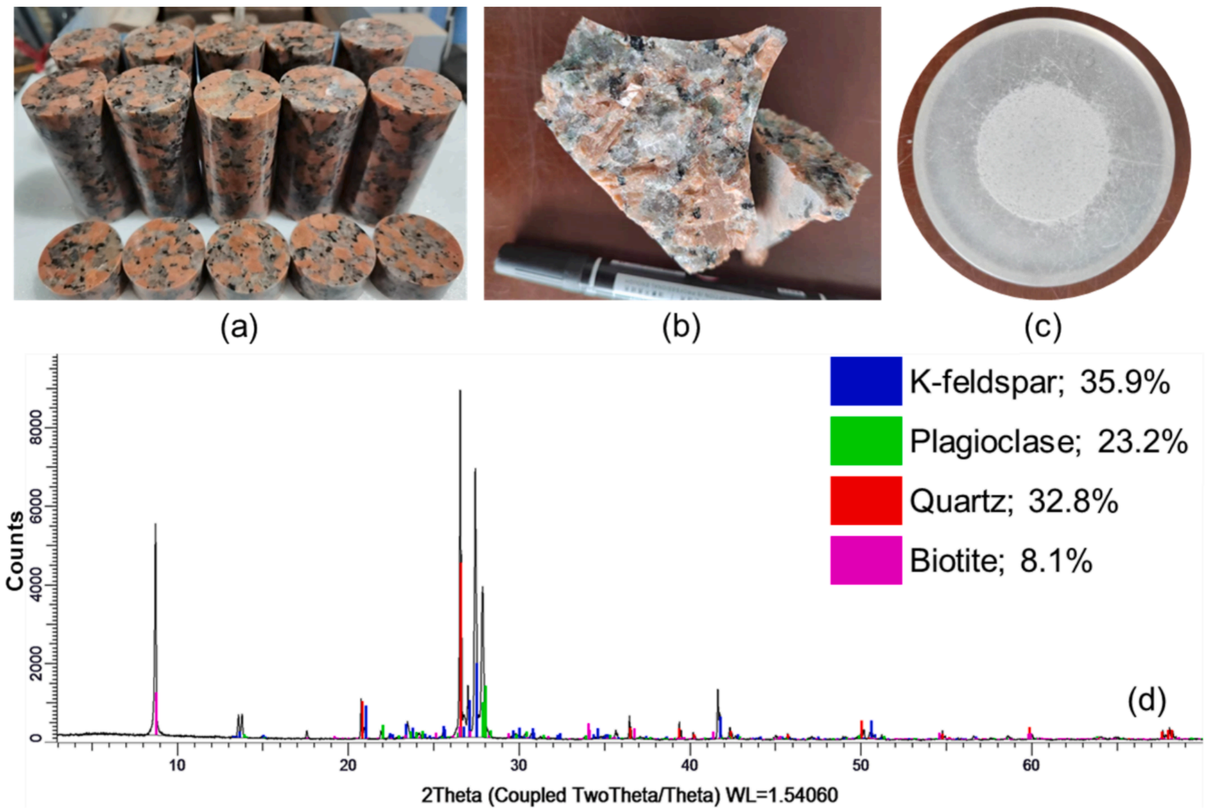

Fig. 3. Individual rock samples and XRD results.

inadequately defined.

While laboratory techniques such as CT and SEM enable the observation of microstructures in granites, they lack a consistent view of the genesis of granites from which microcracking can then grow (Chen et al., 2015; Zhuang et al., 2022; Sufian and Russell, 2013). With the rapid advancement of computational science, numerical simulation methods have gained increasing prominence in defining evolving textures. Numerical simulations, calibrated against experimental observations can effectively address the limitations inherent in traditional experimental approaches (Wang et al., 2014, 2017; Jing, 2003; Huang et al., 2023).

The Particle-Distinct Element Method (Particle-DEM) offers distinct advantages over finite element and other continuum-mechanics methods in simulating the microscopic damage through failure response of brittle rocks (Potyondy, 2004; Wang et al., 2023). Prior studies focusing on microscopic damage and crack propagation of brittle crystalline rocks utilizing the Particle-DEM approach have employed Grain-Based Models (GBM) to characterize the microscopic mineral composition and structure of crystalline rocks (Potyondy, 2010; Hu et al., 2023). However, GBM models exhibit three notable deficiencies (Hofmann et al., 2015a; Saadat and Taheri 2020): These are: 1) The generation of mineral grains within the GBM relies on Voronoi tessellation, resulting in grain boundaries that are restricted to fixed convex polygons. This limitation fails to accurately replicate the pronounced self-locking effects observed between mineral grains in real-world deformation scenarios; 2) The GBM model does not allow for alterations in grain shape, thereby neglecting anisotropic characteristics related to both shape and orientation of mineral grains; and 3) The contact model for grain boundaries within GBMs typically employ a uniform set of mechanical parameters – but this approach overlooks variations in mechanical properties at interfaces between different minerals under realistic conditions. Some studies have developed a novel GBM using digital image processing techniques that can accurately characterize the microstructure of granite. However, this method demands sophisticated preprocessing techniques and smaller sub-grain sizes, potentially increasing computational time (Zhou et al., 2025; Guo et al., 2023a; 2023b).

In addressing the limitations of GBM models, this study introduces a novel method to characterize the microstructural features of granites, termed a Grain-Texture Model (GTM). We offer a comprehensive description of this model generation process and parameter calibration, validating the accuracy of this novel approach in simulating the mechanical properties and failure characteristics of granites through comparison with experimental results. We then provide an in-depth analysis of how biotite content, strength and stiffness influence the mechanical properties and failure characteristics of the ensemble granite aggregate. Finally, we elucidate how variations in mineral shape and orientation impact these macroscale mechanical properties and failure characteristics by generating four distinct mineral shapes alongside five different angular orientations.

2. Grain-texture model

The heterogeneity and anisotropy of mineral grains in granite significantly influence both the macro- and micro-scopic mechanical properties, as well as the crack initiation and ultimate failure characteristics of rocks (Hu et al., 2024; Lan et al., 2010; Peng et al., 2017, 2021). The following introduces a novel method for characterizing the microstructural features of minerals in granites via the “templated” – “grain growth” method. This method enhances the ability of the model to characterize the self-locking effect of mineral grains while also accounting for the influences of grain shape and orientation on anisotropic behavior.

We begin a comprehensive introduction to the detailed procedures of the novel method for modeling the GTM; subsequently, microscopic parameters are calibrated through comparative analysis with experimental results. Finally, the GTM model is applied in numerical simulations of uniaxial compression, triaxial compression and direct tensile experiments to explore the evolution of failure mechanisms and

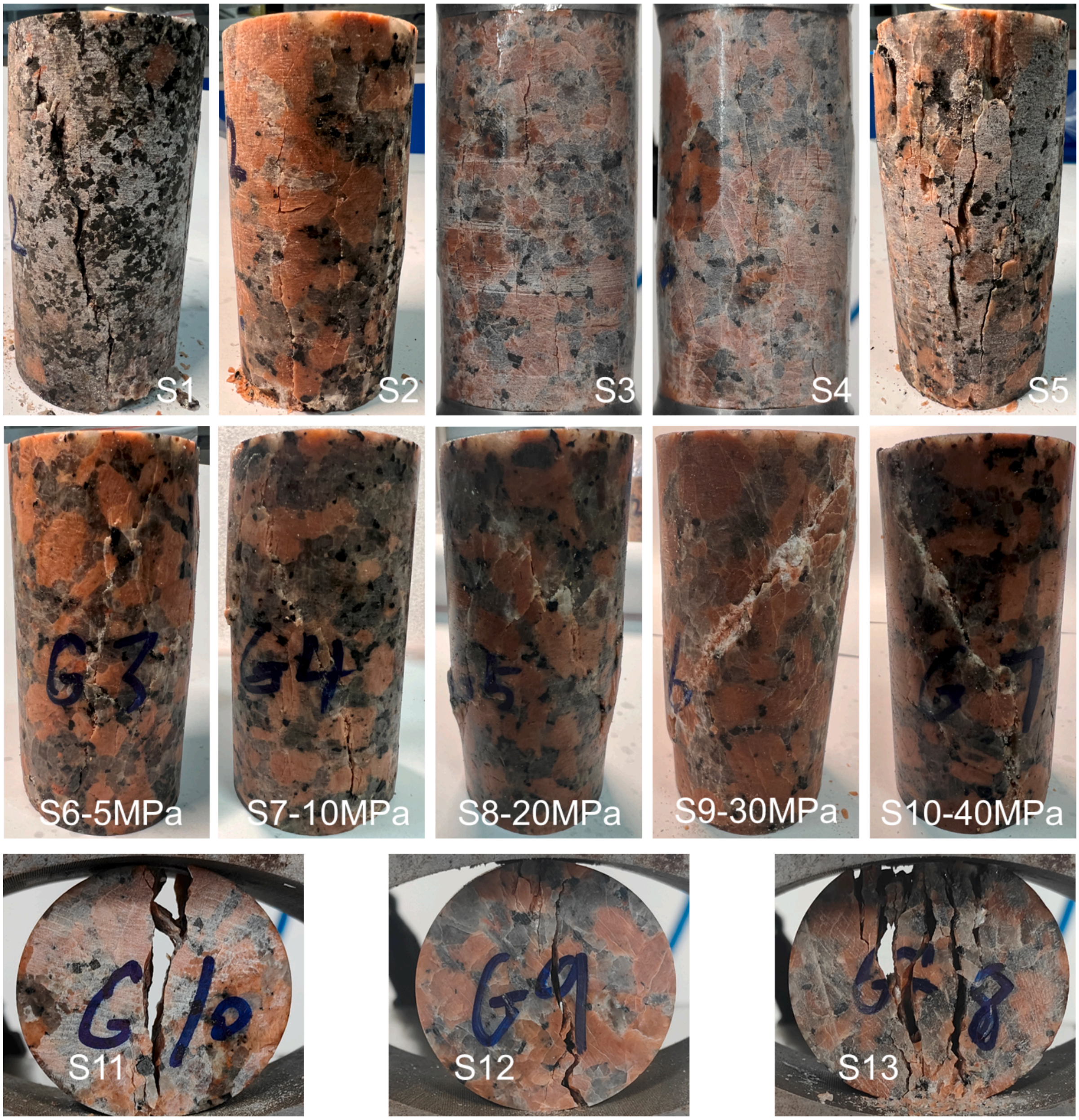

Fig. 4. Failure characteristics of granite specimens under various loading conditions. S1-S5: Uniaxial compression test; S6-S10: Triaxial compression test; S11-S13: Brazilian tensile test.

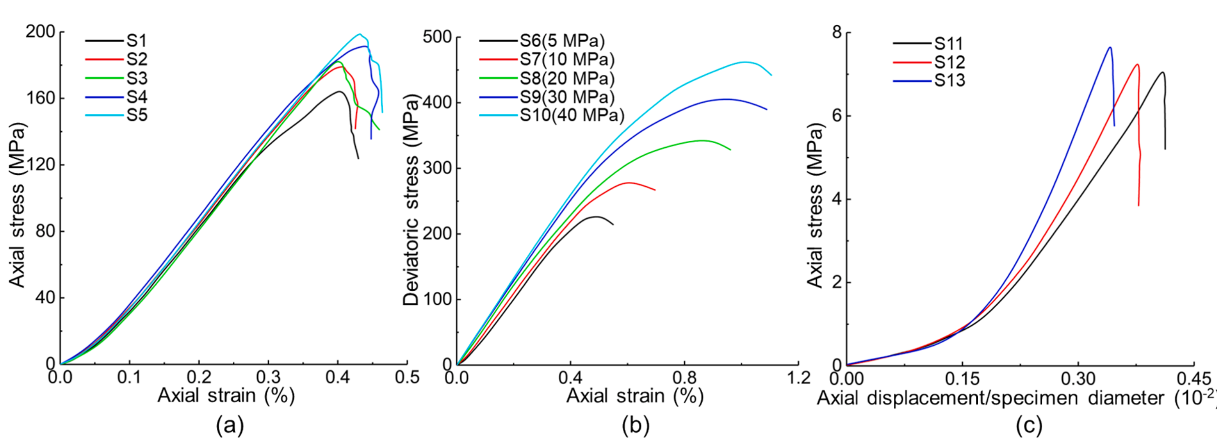

Fig. 5. Stress–strain curves for rock samples: (a) Uniaxial compression test; (b) Triaxial compression test; and (c) Brazilian tensile test.

Table 1
Experimental results for granite samples.

Uniaxial compression test	Granite specimens	S1	S2	S3	S4	S5
	UCS (MPa)	164.5	179.1	182.4	191.1	199.3
	Elastic Modulus (GPa)	54.5	55.5	53.3	56.4	56.8
	Poisson ratio	0.214	0.180	0.197	0.203	0.221
Triaxial compression test	Confining stress (MPa)	5	10	20	30	40
	Compression strength (MPa)	231.8	289.5	363.2	437.0	493.1
Brazilian tensile test	Granite specimens	S11	S12	S13	–	–
	TS (MPa)	7.1	7.3	7.6	–	–

mechanical properties from a microscopic perspective.

2.1. "Templated" and "grain growth" method

The GBM method divides the Voronoi tessellation with the positions of pre-generated random grain seeds, subsequently identifying and grouping the sub-grains based on the tessellation grid to model the microstructure, as illustrated in Fig. 1a–c. As shown in Fig. 1d, while this method effectively represents various mineral structures, it constrains all mineral shapes to fixed convex polyhedra that cannot be altered, thereby inadequately capturing the self-locking effect inherent in minerals (Potyondy, 2010).

The Flat-joint contact model (FJM), proposed by Potyondy (2012), incorporates a conceptual bonding interface to enhance the self-locking effect within the particle model. While the FJM model provides a more accurate representation of mineral grains, the Linear parallel bond model (LPBM) better captures the mechanical behaviors of grain boundaries – including phenomena such as opening, sliding, and deflection. For further details regarding both the FJM and LPBM, please refer to our prior work (Wang et al., 2024a; 2024b).

As illustrated in Fig. 1e–j, the generation of the GTM can be categorized into four distinct steps: (1) Random distribution of grain seeds; (2) Creation of sub-grain numerical samples; (3) "templated" – "grain growth" of grain clusters; and (4) Identification of contact groups.

(1) **Random distribution of grain seeds:** As illustrated in Fig. 1e, particles of varying colors correspond to different mineral types. The first step involves generating a random grain seed model based on the size, composition and proportion of each mineral present in the target rock. The dimensions, composition and proportions of the random grain seeds are consistent with the proportions in the target rock. Following the generation of the random grain seed model, information regarding the grouping, position, and size of each grain seed is saved.
(2) **Creation of sub-grain numerical samples:** As illustrated in Fig. 1f, to achieve a more accurate and realistic microstructural representation of the mineral, smaller sub-grain sizes yield better results. However, reducing the sub-grain size increases the number of grains significantly, thereby greatly extending computation time. Consequently, it is essential to strike a balance between computational efficiency and the authenticity of the microstructural representation when determining sub-grain size. Typically, the sub-grain size is defined as the smallest grain size present within the mineral.
(3) "**Templated" – "grain growth" of grain clusters:** As illustrated in Fig. 1g, the sub-grain numerical sample generated in Step (2) is 'templated' based on the grouping, position, and size information of the random grain seed model obtained in Step (1). The mineral grain clusters are delineated such that their areas correspond to those of the grain seeds. In the GTM, grain clusters can assume an elliptical shape; their shape and orientation can be manipulated by rotating the local coordinate system and adjusting its major and minor axes. This methodology will be elaborated upon when discussing how biotite grain shape and orientation influence rock mechanical properties. However, following the 'templating'

Table 2
Macroscopic mechanical properties of mineral grains (Hofmann et al., 2015b; Li et al., 2018; Yang et al., 2020; Zhou et al., 2019).

Macroscopic mechanical properties	K-feldspar	Plagioclase	Quartz	Biotite
Elastic Modulus (GPa)	48.7	55.3	63.1	35.1
Experimental results	45–85	45–75	60–90	35–180
TS (MPa)	30	35	50	18
Experimental results	11–35	35	30–50	5–40
UCS (MPa)	192.7	202.4	327.6	98
Experimental results	180–450	180–450	200–700	80–260

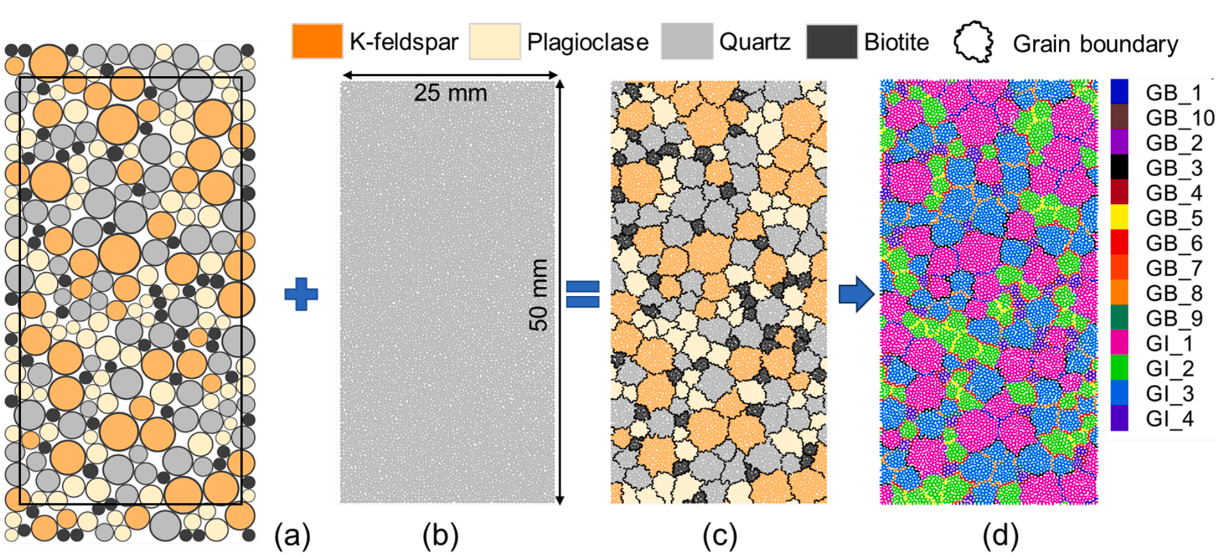

Fig. 6. Procedure for modeling the GTM of granite: (a) Distribution of random grain seeds; (b) Sub-grain specimen; (c) GTM sample; and (d) Contact groups. GB: Grain boundary; GI: Intra-grain.

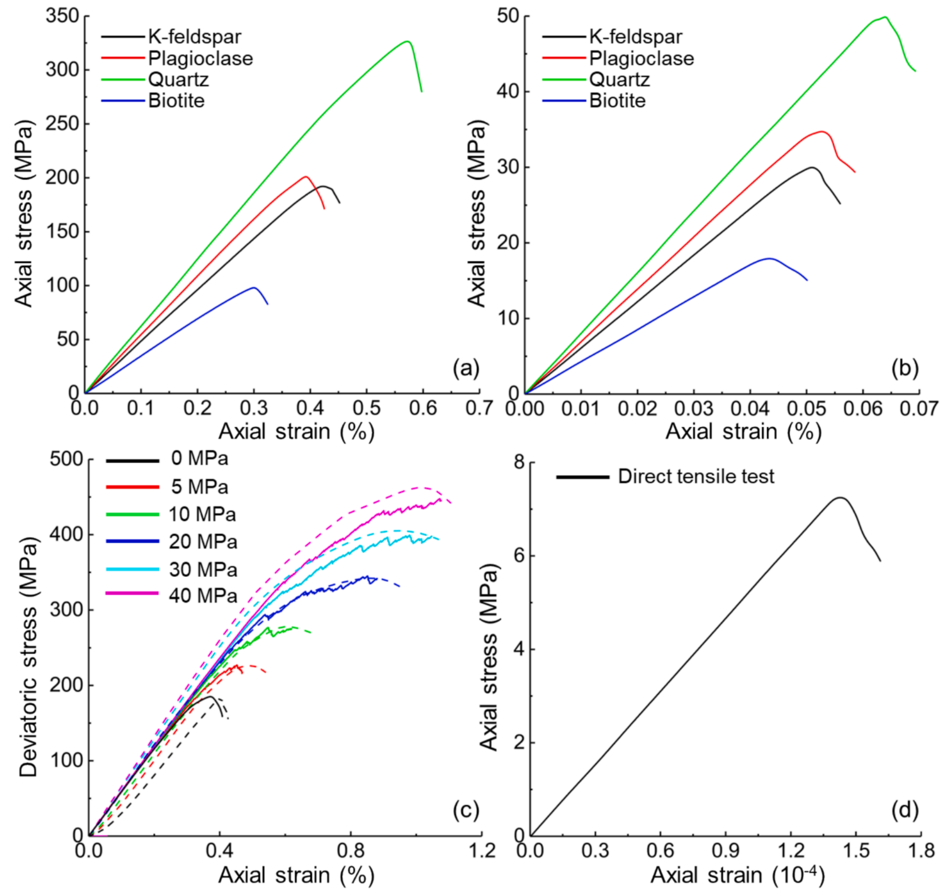

Fig. 7. Stress–strain curves for compression and tensile tests for mineral grains and rock samples. (a) and (b): Mineral grains; (c) and (d): Rock samples. The dashed line represents the experimental results and the solid line represents the numerical results.

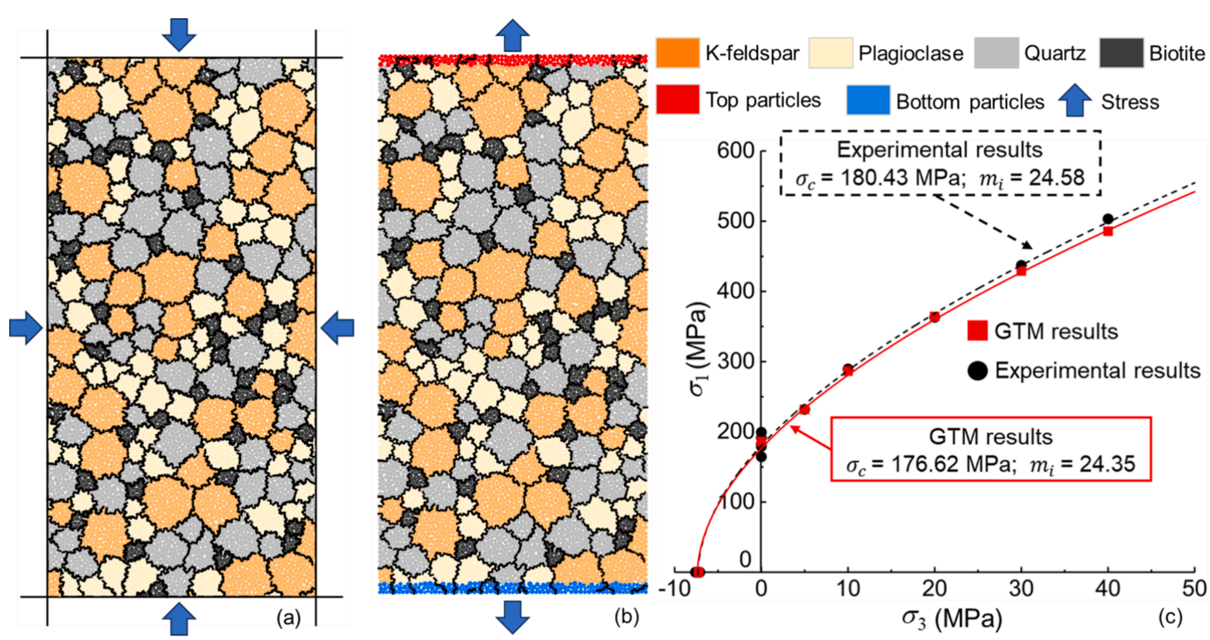

Fig. 8. Numerical sample used in: (a) Compression test and (b) Tensile test; (c) Hoek-Brown strength envelope of experimental and GTM results.

process for the grain cluster, as depicted in Fig. 1h, some 'gap particles' may exist between these clusters. These particles lack assigned mineral group information. The remaining ungrouped 'gap particles' are classified using a 'grain growth' method. Initially, this method defines 'boundary particles' at the edges of each cluster which then expand outward to search for adjacent 'gap particles'. Once identified by 'boundary particles', these 'gap particles' become part of the cluster boundary, allowing it to

Table 3
Microscopic mechanical parameters for mineral grains and grain boundaries.

Microscopic mechanical parameters	K-feldspar	Plagioclase	Quartz	Biotite
Volume fraction (%)	36	23	33	8
Minimum mineral size (mm)	2	1.5	2	1.5
Maximum mineral size (mm)	5	3	4	1.5
Density (kg/m^3)	2600	2600	2650	2750
Contact Elastic Modulus (GPa)	52	55	65	35
Contact stiffness ratio	1.6	1.6	1.0	2.0
Contact friction coefficient	0.6	0.6	0.6	0.6
Contact tensile strength (MPa)	42	39	56	23
Contact cohesion (MPa)	146	143	203	68
Contact frictional angle (°)	42	42	55	38
Element number	4			
Minimum sub-grain radius (mm)	0.15			
Radius ratio	1.66			
Modulus coefficient	0.9			
Stiffness ratio coefficient	2.0			
Friction coefficient	1.0			
Cohesion coefficient	0.7			
Friction angle coefficient	1			
Tensile strength coefficient	0.25			

continue expanding outward iteratively until all 'gap particles' are incorporated into their respective clusters, as shown in Fig. 1i.

(4) **Identification of contact groups:** Following the allocation of all particles to their respective grain clusters, parameters for both GI and GB contacts are assigned. Notably, the nature of GB contacts is more intricate; thus. A grouping algorithm is employed to identify the contact grouping information of the particles on either side of these grain boundaries, facilitating the determination of their corresponding contact groups. GBMs treat all grain boundary contacts as uniform (Fig. 1c), whereas the GTM employs a contact identification algorithm to differentiate between various types of GB contacts (Fig. 1j).

Fig. 2 illustrates the four mineral grain contact patterns identified by Ulusay et al. (1994) in crystalline rocks and it was demonstrated that these contact patterns significantly influence mechanical properties, including rock strength. The GTM accurately replicates all four contact patterns using the "templated" – "grain growth" modeling approach. In contrast, the traditional GBM, which employs Voronoi grid partitioning, is limited to reproducing only the straight contact pattern (Fig. 1c).

2.2. Mesoscopic parameter calibration based on experimental results

We acquire the physical and mechanical properties of granite through a series of rock mechanical deformation experiments. Subsequently, a GTM, incorporating its authentic mineral structure based on granite, is developed and calibrated in accordance with the experimental results. Finally, this GTM undergoes both compressive and tensile testing to investigate its mechanical behavior and fracture characteristics at the microscopic scale.

2.2.1. Experimental results for granite

Crystalline rocks, exemplified by granite, are generally comprised of various mineral grains at the microscopic scale. The heterogeneity and anisotropy of the granite microstructure significantly influence its macroscopic mechanical properties and failure response. We focus on porphyritic monzogranite, with a series of experiments conducted to ascertain the macroscopic mechanical characteristics and microstructure, thereby providing a foundation for the development of the GTM numerical model and the calibration of its microscopic parameters.

Different types of granite exhibit distinct macroscopic mechanical properties due to variations in the physical and mechanical characteristics of mineral grains as well as their microstructural features. This study focuses on testing the physical and mechanical properties of porphyritic granite while calibrating its corresponding microstructural mechanical parameters. The primary mineral composition and content within the granite can be determined through X-ray diffraction (XRD) spectroscopy (Fig. 3d). Based on XRD results, the main mineral composition and respective contents in the granite sample are: K-feldspar (35.9 %), plagioclase (23.2 %), quartz (32.8 %), biotite (8.1 %).

Standard cylindrical samples measuring 100 mm in height and 50 mm in diameter were subjected to uniaxial and triaxial compression tests, while a standard sample with a diameter of 50 mm and a thickness of 25 mm was prepared for Brazilian tensile tests (Fig. 3a). The experiments were conducted using the RTR-1500 rock triaxial apparatus. The axial loading rates for both the uniaxial and triaxial compression tests were set at 0.12 mm/min, whereas the loading rate for the Brazilian tensile test was established at 0.5 kN/s. The failure characteristics of the granite samples post-testing are illustrated in Fig. 4. Under uniaxial compression, the rock sample split in brittle failure. This was

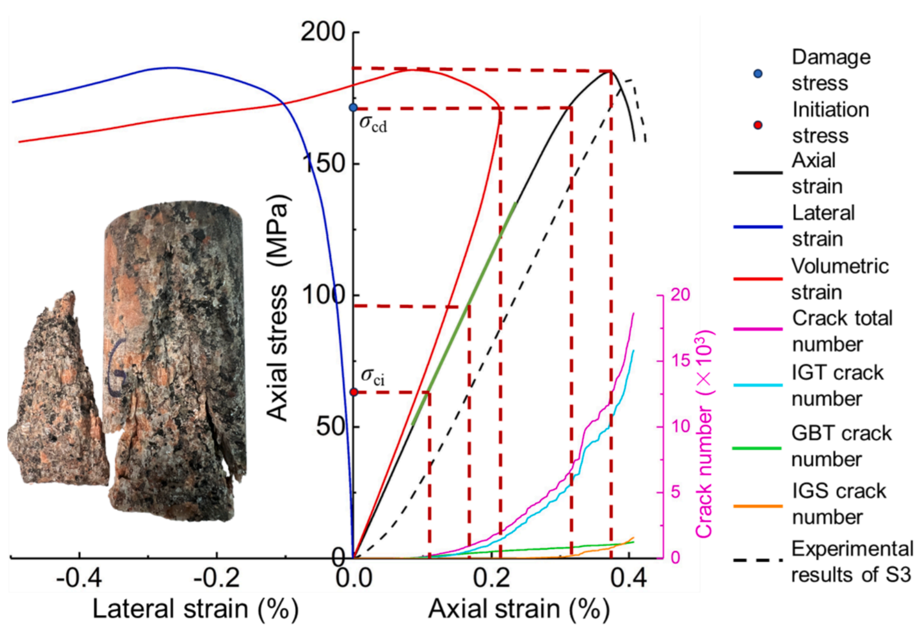

Fig. 9. Stress–strain curve and variation in crack number during the uniaxial compression test.

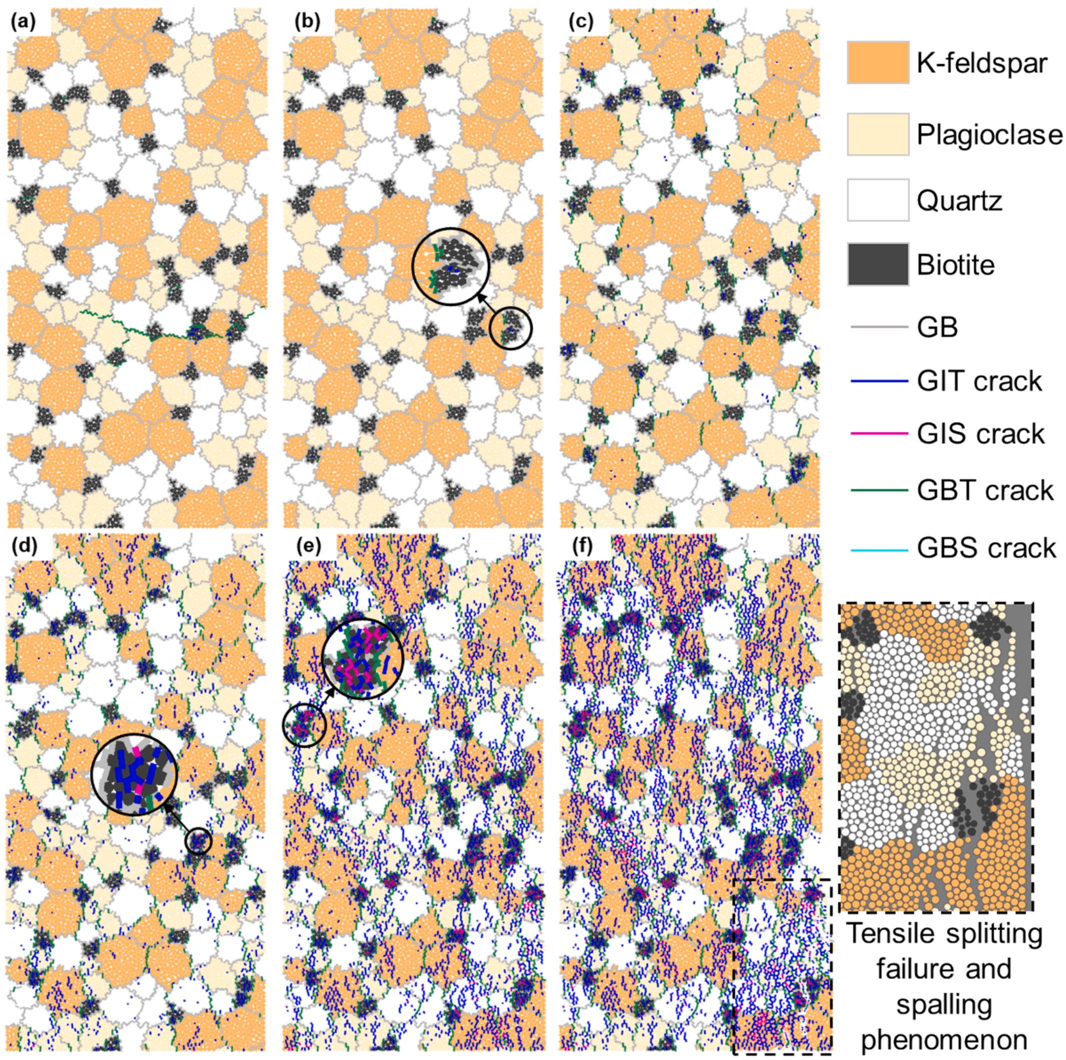

Fig. 10. Results of the GTM showing crack distribution under uniaxial compressive loading at various axial stress stages: (b) 30%, (c) 50%, (d) 75%, (e) σ_{pk}, and (f) Post-peak as well as (a) Tensile test. *GB: Grain boundary; GI: Intra-grain; T: Tensile; S: Shear.

characterized by distinct vertical tensile cracks along with localized block spalling; additionally, intra-grain (GI) cracking was significant. In contrast, under triaxial compression and at low confining stress, the rock sample exhibited similar tensile failure characteristics as observed in the uniaxial compression test; however, as confining stress increased, there was a marked transition from tensile to shear failure accompanied by the development of prominent macroscopic shear cracks.

The stress–strain curves for the rock samples subjected to compression and Brazilian tensile tests are presented in Fig. 5. The macroscopic mechanical parameters for granite, including compressive strength, tensile strength (TS), and elastic modulus, are detailed in Table 1. The average uniaxial compressive strength (UCS) of the rock samples is ~183.3 MPa, with an elastic modulus of ~55.5 GPa and a tensile strength of ~7.33 MPa. The triaxial compressive strengths at confining stresses of 5 MPa, 10 MPa, 20 MPa, 30 MPa, and 40 MPa are of 226.8 MPa, 279.5 MPa, 339.3 MPa, 407.0 MPa, and 463.1 MPa respectively.

2.2.2. Calibration procedures

The specific procedure for constructing the GTM numerical model is illustrated in Fig. 6. First, a seed model with larger model size is created according to the mineral grain data (Fig. 6a). The mineral grain size distribution is as follows: K-feldspars range from 2.0 to 5.0 mm, plagioclase from 1.5 to 3.0 mm, quartz from 2 to 4.0 mm, and biotite at a consistent size of 1.5 mm. Subsequently, a sub-grain specimen measuring 50 mm by 25 mm is established (Fig. 6b), with a minimum sub-grain radius of 0.15 mm, a size ratio of 1.66, and a total particle count of 9 017. Fig. 6c depicts the GTM numerical model of the granite; this model incorporates four types of minerals along with four GI contact groups and ten GB contact groups (Fig. 6d).

The calibration process for the GTM model is grounded in the calibration methodology established by Zhou et al., 2017, 2019. This process is systematically divided into two steps: 1) the calibration of FJM parameters for mineral grains; and 2) the calibration of LPBM parameters for grain boundaries:

1) Calibration of FJM parameters for mineral grains

In the calibration process for FJM parameters, we sequentially select three macroscopic mechanical parameters: elastic modulus, tensile strength and compressive strength. The elastic modulus for the minerals is initially calibrated by establishing an infinite contact strength, followed by continuous adjustments to the contact elastic modulus. Subsequently, the macroscopic tensile strength of the minerals is calibrated through adjustments to the contact tensile strength within the FJM. It is important to note that while the contact tensile strength significantly influences both tensile and compressive strengths, other factors such as cohesion and friction angle have a lesser effect on TS but a pronounced impact on UCS; thus, calibration for compressive strength occurs last. Finally, this parameter is refined by adjusting cohesion with an initial friction angle set at 0°. The friction angle exerts minimal influence on

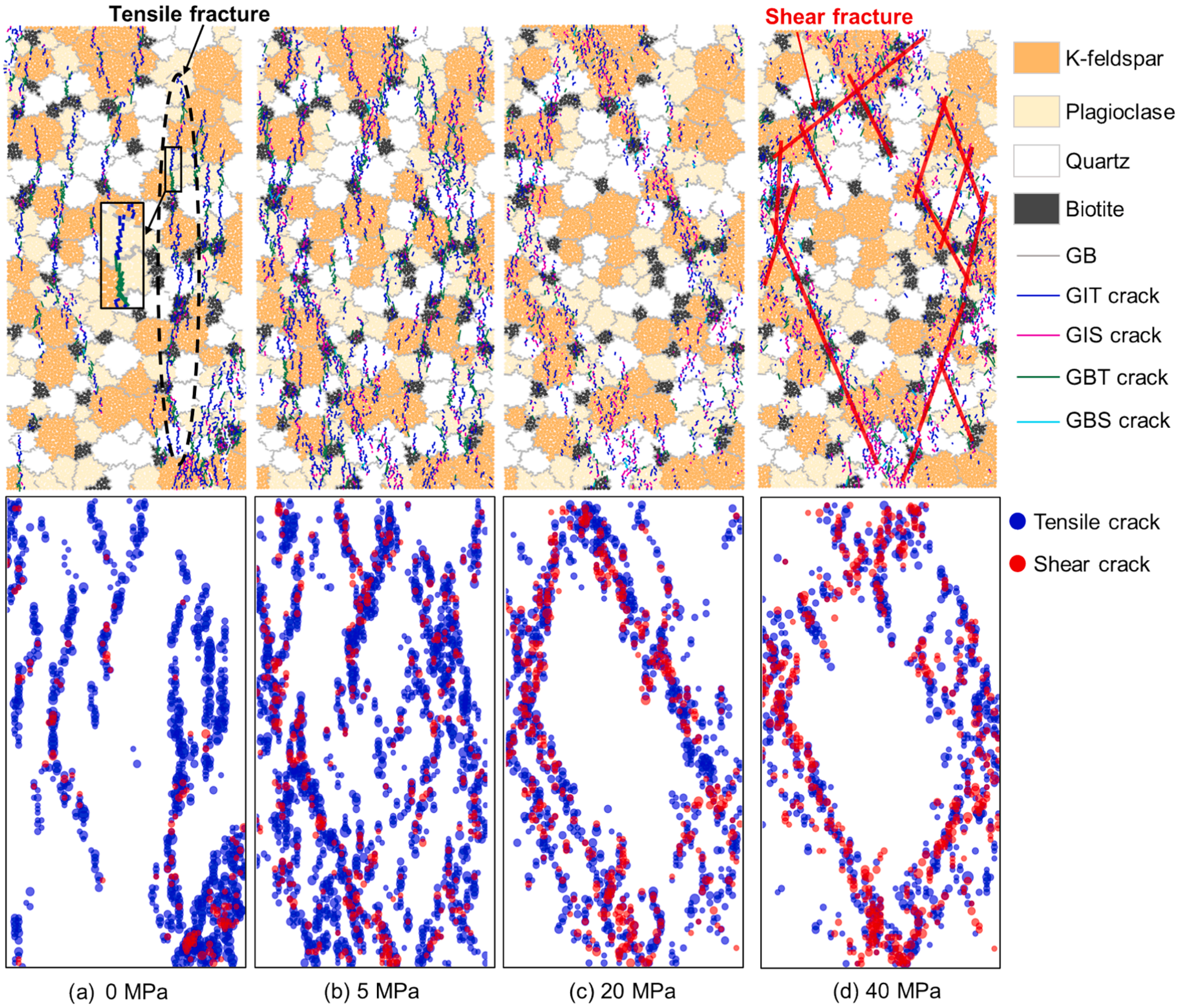

Fig. 11. Distribution of cracks (with apertures exceeding 0.01 mm) at varying confining stresses. *GB: Grain boundary; GI: Intra-grain; T: Tensile; S: Shear.

UCS but has a more substantial effect on triaxial compressive strength; therefore, it requires calibration based on triaxial compressive test results.

2) Calibration of LPBM parameters for grain boundaries

The LPBM parameters are defined as the product of the corresponding reduction coefficients and the FJM parameters of adjacent minerals sharing a common boundary. Calibration is performed using a trial-and-error approach, incorporating macroscopic elastic modulus, Poisson ratio, TS, UCS, and the Hoek-Brown strength criterion parameter m_i. The following relationships characterize the interactions between microscopic and macroscopic mechanical parameters at grain boundaries: 1). Poisson ratio is primarily influenced by the stiffness ratio reduction coefficient; since the stiffness of the grain boundary contact is lower than that of the intra-grain contact. This results in a modulus reduction coefficient less than 1. Conversely, due to greater lateral deformation at grain boundaries, the stiffness ratio reduction coefficient exceeds 1; 2). TS is predominantly affected by its respective tensile strength reduction coefficient; 3). UCS is influenced by cohesion reduction coefficients while parameter m_i from the Hoek-Brown criterion relates to internal friction angle reduction coefficients.

2.2.3. *Calibrated results*

During the parameter calibration for the four minerals, all contacts within the sub-grain numerical model depicted in Fig. 6b were assigned the mechanical parameters of a single mineral. The macroscopic mechanical properties were then numerically derived from uniaxial compression and tensile tests. The macroscopic mechanical characteristics of the four minerals are presented in Table 2, while the numerical test results are illustrated in Fig. 7a and b. The macroscopic mechanical properties for all minerals fall within the range established by the experimental results (Hofmann et al., 2015b; Li et al., 2018; Yang et al., 2020; Zhou et al., 2019).

Following the calibration of the mineral parameters, the parameters representing grain boundaries were further refined through compressive and direct tensile tests on granite samples, as illustrated in Fig. 8a and b. In Fig. 8b, the direct tensile test involved segmenting the 2.5 mm thick particles at both ends of the model into groups and applying axial tensile forces by moving them outward. Through extensive trial-and-error iterations, the microscopic mechanical parameters of granite are detailed in Table 3.

The stress–strain curves of granite presented in Fig. 7c and d, obtained from compression and tension tests, demonstrate that the GTM effectively replicates the macroscopic mechanical properties obtained in the experiments. Analysis of the compression test results reveals that as confining stress increases, the stress–strain curve exhibits a characteristic brittle-ductile transition: under uniaxial compression and low confining stresses, the post-peak stage displays pronounced strain softening behavior; conversely, with rising confining stresses, the frictional effects within the rock intensify, leading to significant strain hardening in the post-peak stage and exhibiting a dual stiffness. The GTM

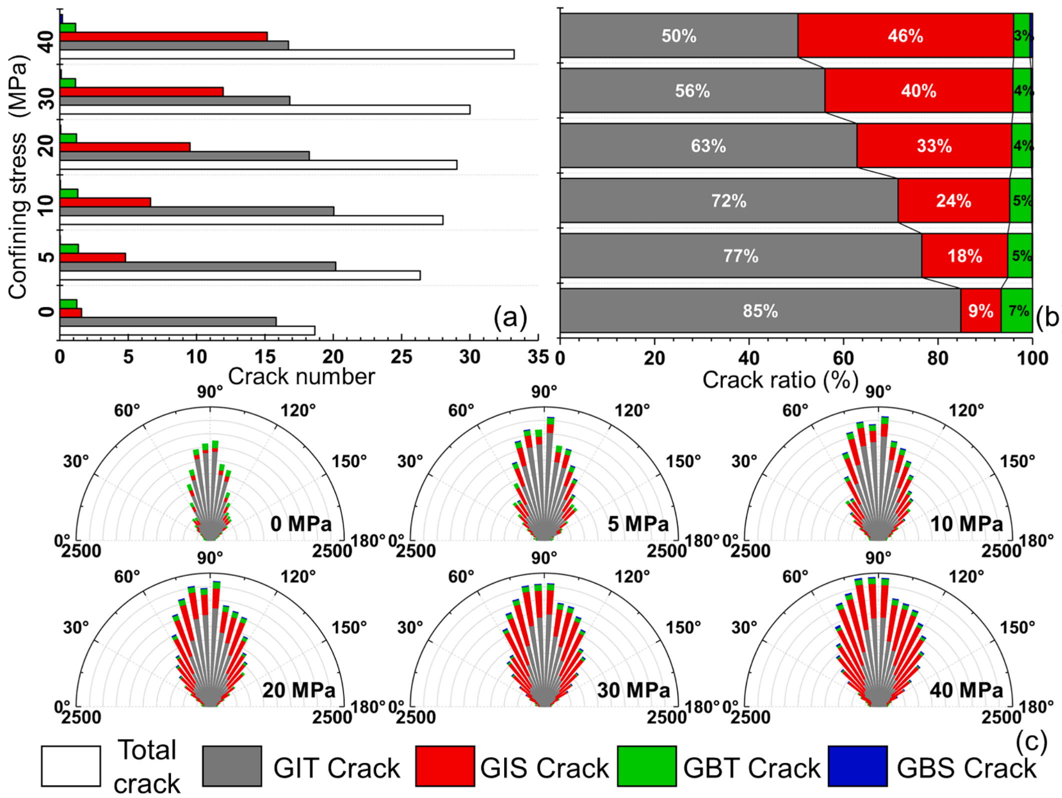

Fig. 12. Statistical results for cracks evolving under varying confining stresses: (a) Number of different crack types; (b) Proportion of different crack types; (c) Rose diagram of crack orientations. *GB: Grain boundary; GI: Intra-grain; T: Tensile; S: Shear.

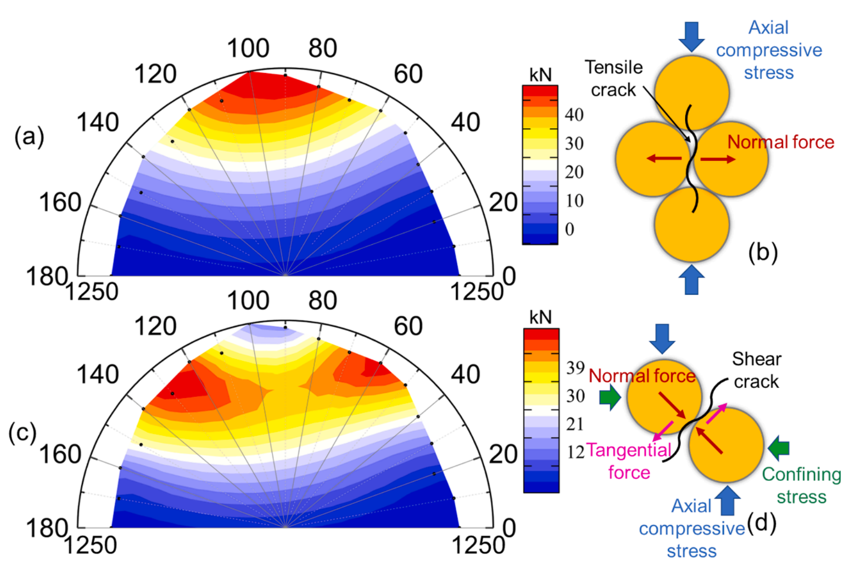

Fig. 13. Uniaxial compression: (a) Rose diagram of normal contact force; (b) Tensile failure mechanism. At 40 MPa confining stress: (c) Rose diagram of tangential contact forces; (b) Shear failure mechanism.

successfully captures this brittle-ductile transition behavior.

The Hoek-Brown strength criterion has been extensively utilized to characterize peak strength under varying confining pressures. This criterion is defined as follows (Hoek and Brown, 1997):

$$\sigma_1 = \sigma_3 + \sigma_{ucs}(m_i\sigma_3/\sigma_{ucs} + s)^{0.5} \quad (1)$$

where, σ_{ucs} denotes the UCS; σ_1 and σ_2 represent the peak strength and confining stress, respectively; m_i and s signify the intrinsic material properties of the rock mass structure, with intact rock defining s as 1.

Fig. 8c illustrates the Hoek-Brown strength envelope for both the experimental and GTM results. The m_i obtained from experimental results is 24.58 and for the GTM is 24.35.

2.3. Numerical results for grain-texture model

The GTM derived from the aforementioned calibration process was employed to conduct both compression and tensile numerical experiments on the virtual specimen to explore the mechanical properties,

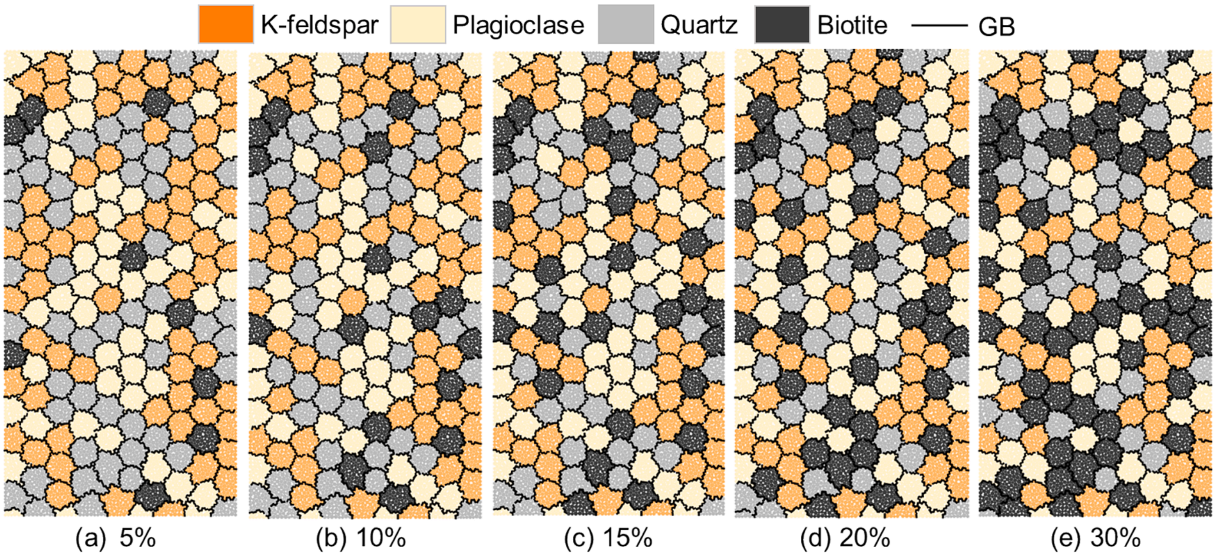

Fig. 14. Granite GTM model with varying biotite content.

Table 4
Mineral content information for the model.

Case	K-feldspar (%)	Plagioclase (%)	Quartz (%)	Biotite (%)
1	31.67	31.67	31.66	5
2	30	30	30	10
3	28.34	28.33	28.33	15
4	26.67	26.67	26.66	20
5	23.34	23.33	23.33	30

failure characteristics, and microscopic crack propagation behavior of granite.

2.3.1. Uniaxial compression test and direct tensile test

The stress–strain curve and variation in crack number during uniaxial compression are illustrated in Fig. 9. Under uniaxial compression, the granite exhibits two characteristic stresses: an initiation stress σ_{ci} and a damage stress σ_{cd}. In this study, the σ_{ci} value corresponds to 1 % of the total number of cracks post-peak (Wang et al., 2024a). The σ_{cd} value is taken as the axial stress at which maximum volumetric strain occurs. Specifically, σ_{ci} and σ_{cd} correspond to 33.8 % and 89.3 % of peak strength σ_{pk}, respectively. Prior to reaching σ_{cd}, crack numbers increase steadily; however, once axial stress exceeds σ_{cd}, the number of cracks begin to grow rapidly until reaching σ_{pk}. Throughout the entire uniaxial compression loading process, tensile cracks within minerals predominate. Conversely, after surpassing σ_{cd}, shear cracks emerge within these minerals such that their quantity exceeds that of tensile cracks at mineral boundaries following the post-peak stage. Shear cracks located at grain boundaries are too sparse to be represented in Fig. 9.

Fig. 10 shows the crack distribution observed in uniaxial compression tests across various axial stress stages (30 %, 50 % and 75 % of peak, and post-peak) as well as in tensile tests. At the 30 % axial stress stage, cracks have initiated; from a magnified view, it is evident that the first cracks to emerge are tensile cracks situated at biotite grain boundaries, attributed to the relatively low strength of the biotite. At the 50 % axial stress stage, an increased number of GB tensile cracks manifest beyond the biotite boundaries, with internal tensile cracks also beginning to develop within minerals—primarily within biotite itself. At the 75 % axial stress stage, numerous GB tensile cracks have penetrated the mineral while many unpenetrated tensile cracks remain present within minerals; additionally, the magnified view reveals emerging shear cracks within the biotite that is increasingly fragmented, compared to those found in other minerals. During the peak axial stress stage, a greater prevalence of shear cracks appears within the biotite; concurrently, several feldspar minerals experience penetration by internal tensile fractures resulting in GI cracking. In the post-peak axial stress stage, macroscopic tensile fracture occurs in the sample; however, due to the superior strength characteristics of quartz, fewer internal fractures are observed—furthermore, localized magnification indicates notable bulging and partial spalling phenomena.

The results of the tensile test indicate that a macroscopic tensile crack is manifest horizontally along the grain boundary at the center of the sample, resulting from the application of vertical tensile forces. Additionally, localized tensile cracks are observed within the biotite in proximity to the macroscopic crack.

2.3.2. Triaxial compression test

As illustrated in Fig. 11, the distribution of cracks under uniaxial compression and varying triaxial compression is presented. The results indicate that as the confining stress increases, the macroscopic failure mode of the rock sample transitions from tensile cleavage to shear failure. Under uniaxial compression loading conditions, both GI and GB tensile cracks within the minerals coalesce to form macroscopic tensile fractures. The morphology of these macroscopic tensile fractures is significantly influenced by biotite grains; most fractures traverse through biotite while only a limited number penetrate quartz minerals. These macroscopic tensile fractures are relatively straight and magnified images reveal that they also display transgranular (blue) and round granular (green) fracture states. At 5 MPa confining stress, there is an increase in the proportion of GI shear cracks, resulting in a mixed failure mode rupture characterized by both macroscopic tensile and shear fractures. At 20 MPa and 40 MPa confinement, microcracks become more dispersed and interconnect to form macroscopic conjugate shear fractures, leading to shear-induced rock failure. In summary, the model effectively replicates experimental results for granite subjected to uniaxial through triaxial compression loading conditions. The crack bubble diagram depicted in Fig. 11 offers a more intuitive representation of failure modes.

Fig. 12a and b shows the number and proportion of cracks under varying confining stresses. As confining stress increases, the shear interaction among particles intensifies, leading to a gradual rise in both the number and proportion of shear cracks. At a confining stress of 40 MPa, the proportion of shear cracks approaches 50 %, whereas at uniaxial compression, this proportion is merely 9 %. Conversely, the number of GB tensile cracks remains relatively constant.

As illustrated in Fig. 13a and c, the radial coordinate of the rose

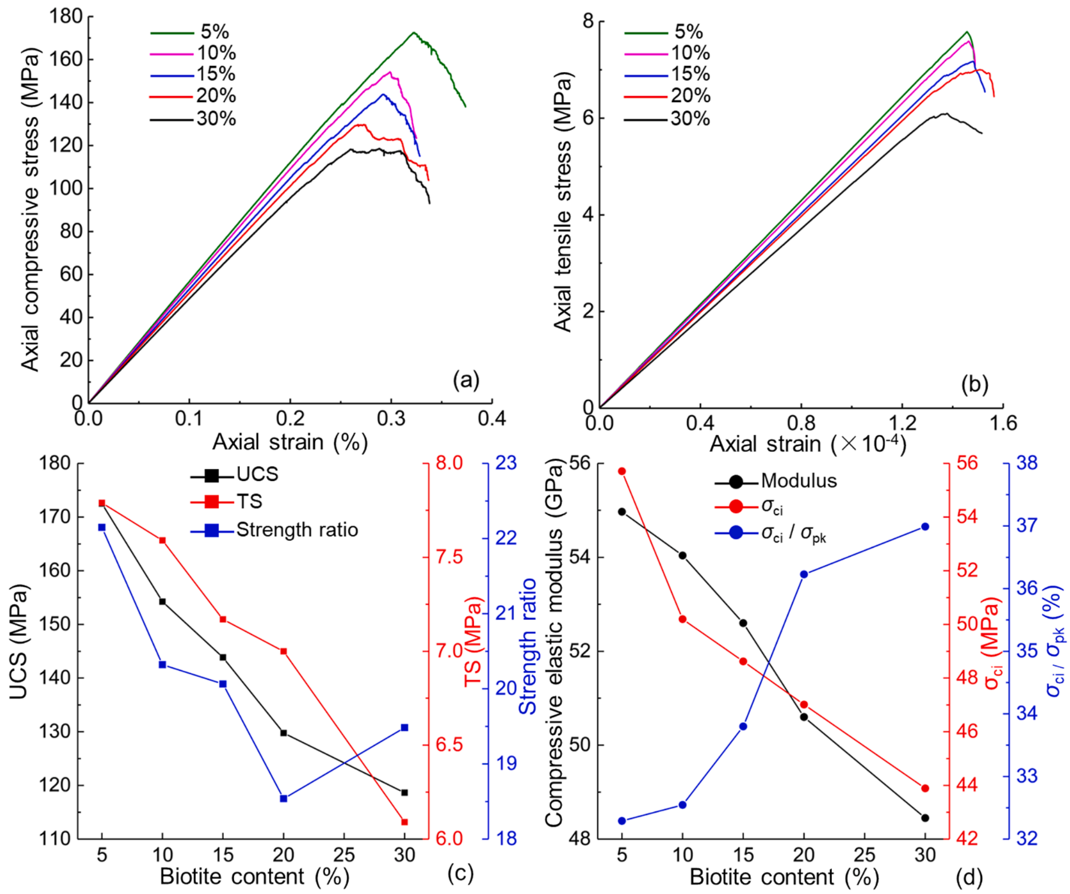

Fig. 15. Influence of biotite content on macroscopic mechanical properties: (a) Uniaxial compression test and resulting stress–strain curves; (b) Tensile test stress–strain curves; (c) Strength; (d) Modulus and characteristic stress.

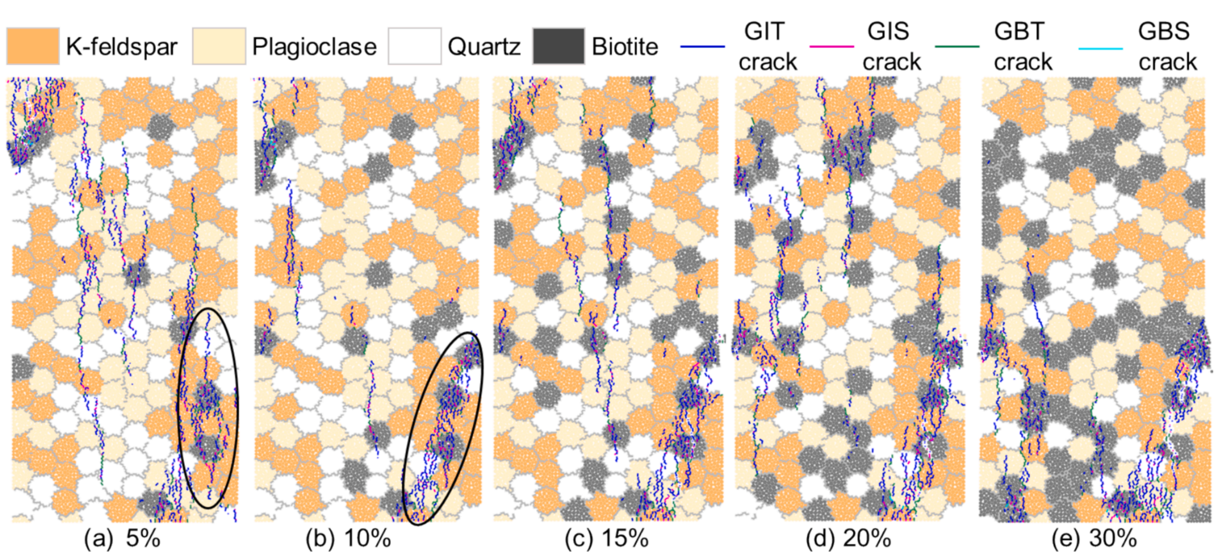

Fig. 16. Crack distribution results for different biotite content models under uniaxial compression (crack apertures greater than 0.01 mm). *GB: Grain boundary; GI: Intra-grain; T: Tensile; S: Shear.

diagram denotes the number of contacts, while the angular coordinate indicates their orientations. The orientations are categorized into 10° intervals for statistical analysis, where both the quantity of contacts and the normal and tangential contact forces associated with each contact are computed for each interval. Subsequently, to determine the average contact force within the statistical interval, we sum all the contact forces and divide by the total number of contacts.

The distribution of normal contact forces under uniaxial compression indicates that the normal contact force between particles increases progressively from the horizontal to the vertical. The tensile failure mechanism (Fig. 13b) elucidates the formation of vertical tensile cracks: when particles are subjected to vertical compressive stress, a horizontal

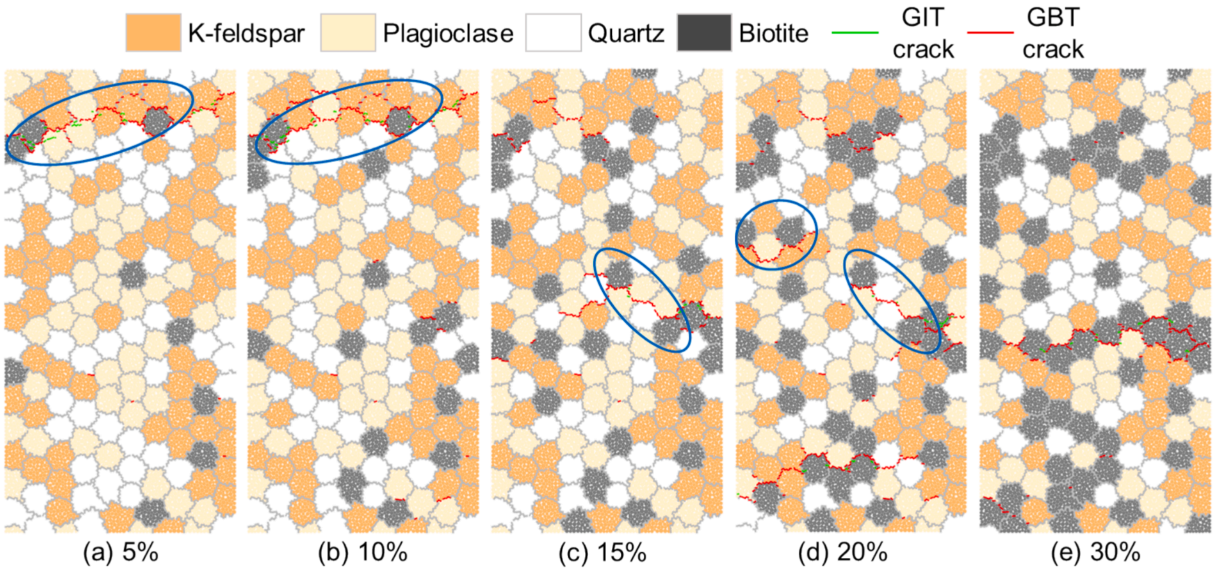

Fig. 17. Crack distribution results for different biotite content models under tension. *GB: Grain boundary; GI: Intra-grain; T: Tensile.

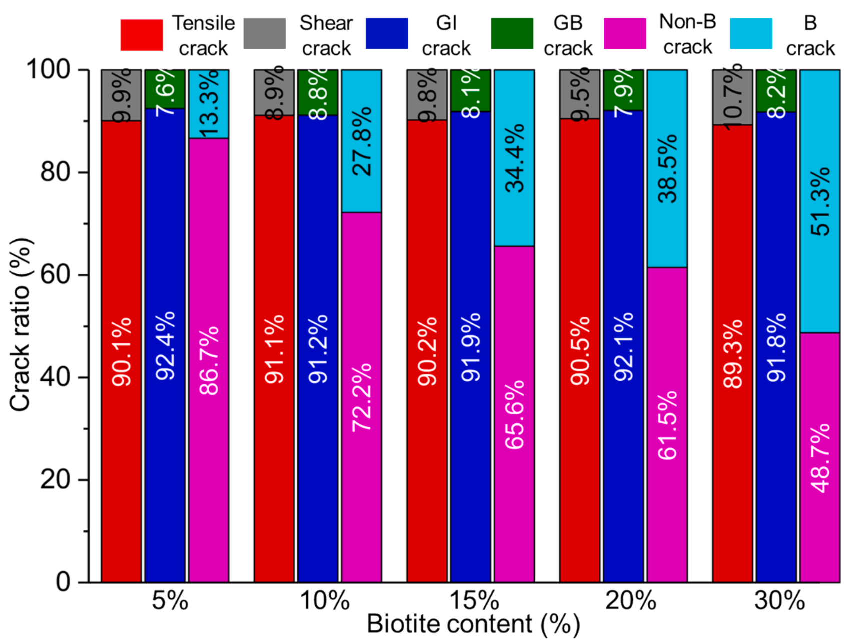

Fig. 18. Crack ratio results for different biotite content models under uniaxial compression. *GB: Grain boundary; GI: Intra-grain; B: Biotite.

tensile force is generated at the vertical contact point, leading to tensile failure in the vertical direction. Under a confining stress of 40 MPa, the tangential contact force attains its maximum value in oblique directions (50°-70°, 120°-140°). The shear failure mechanism (Fig. 13d) further clarifies how oblique shear cracks form under triaxial compression: due to the combined effects of vertical compressive stress and confining stress, oblique contacts experience both normal contact pressure and tangential forces; when these tangential forces reach the shear strength of the contacts, shear failure occurs.

3. Influence of biotite heterogeneity on mechanical and microcracking behavior

The granite GTM effectively captured the mineral grain microstructure and successfully reproduced both the hard and brittle macroscopic mechanical properties as well as the microscopic crack propagation processes. During their formation, crystalline rocks are subjected to complex external conditions that result in highly heterogeneous and anisotropic mineral structural characteristics, with mineral grains exhibiting significant heterogeneity and anisotropy. Due to the heterogeneous mechanical properties of the granite constituent minerals, an increase in the content of soft and weak minerals (such as biotite) resulted in a decrease in the macroscopic mechanical strength of the rock. The significant disparities in the mineral mechanical properties led to a heterogeneous stress field developing within the rock during loading, thereby complicating the microcrack propagation process. We employed the GTM to investigate the effects of biotite heterogeneity (content, strength and stiffness) on the mechanical properties of granite.

3.1. Biotite content

Fig. 14 shows the GTM of granites with varying biotite contents (5 %,

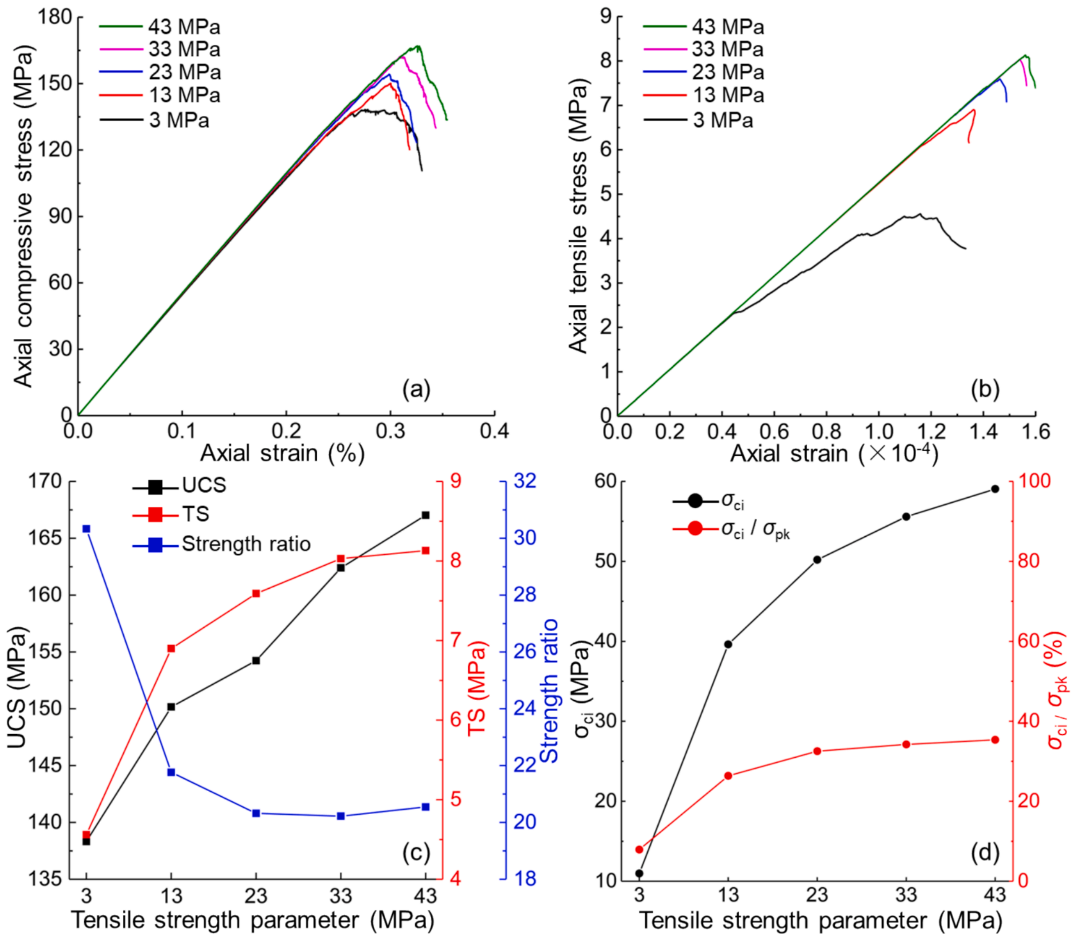

Fig. 19. Influence of tensile strength of biotite on macroscopic mechanical properties: (a) Uniaxial compression test stress–strain curves; (b) Tensile test stress–strain curves; (c) Strength; (d) Characteristic stress.

10 %, 15 %, 20 %, and 30 %). Table 4 provides the mineral content information for the five computational cases. Aside from biotite, the contents of the other three minerals remain constant; furthermore, to mitigate the effects of differences in mineral grain sizes, all minerals are uniformly set to a size of 3 mm. The sub-grain particle model is consistent with that depicted in Fig. 6b, measuring 50 mm by 25 mm, featuring a minimum radius of 0.15 mm, a radius ratio of 1.66 and comprising a total particle count of 9,017.

Fig. 15 illustrates the macroscopic mechanical properties of granite models with varying biotite content. As depicted in Fig. 15a and b, the lower strength and stiffness of biotite relative to other minerals result in a decrease in UCS, TS, and elastic modulus as biotite content increases. At a biotite content of 5 %, the post-peak behavior of the uniaxial compression test exhibits brittle failure; however, this characteristic becomes less pronounced with increasing biotite content.

Fig. 15c illustrates that as biotite content increases, the UCS and compressibility of the rock decrease approximately linearly. The TS also diminishes with increasing biotite content, with a more pronounced reduction observed when biotite content rises from 20 % to 30 %. This phenomenon can be attributed to the increased number of horizontally adjacent biotite grains as their content increases, facilitating the formation of horizontal grain boundary tensile cracks during tensile loading. This further underscore how mineral distribution affects the macroscopic mechanical properties of rocks. The UCS-TS ratio gradually declines as biotite content increases from 5 % to 20 %; however, following an increase in biotite content from 20 % to 30 %, the UCS/TS strength ratio subsequently rises due to a significant drop in TS.

Fig. 15d illustrates that the compressive modulus decreases from 54.97 GPa to 48.45 GPa with increasing biotite content. This reduction is attributed to the lower stiffness of the biotite mineral grains, which tend to experience greater deformation under compression. Furthermore, grain boundary cracks are more likely to develop at the interfaces of biotite, and intra-grain cracking within these grains is also facilitated, resulting in increased deformation of the model. The σ_{ci} gradually diminishes as biotite content rises due to a higher generation of cracks at biotite boundaries during loading. However, the σ_{ci}/σ_{pk} increases with rising biotite content, indicating that the decrease in σ_{ci} is less pronounced than that in σ_{pk}; thus, σ_{pk} is more significantly influenced by biotite content.

The distribution of cracks in granite models with varying biotite content under uniaxial compression is presented in Fig. 16. The GI cracks and GB cracks coalesce to macroscopic fractures. These macroscopic fractures are predominantly parallel to the loading direction (vertical) and all samples exhibit signs of spalling. The presence of biotite significantly influences the morphology of these macroscopic fractures. Due to the relatively low strength of biotite grains, crack initiation tends to occur at biotite boundaries during loading, subsequently expanding and penetrating to form macroscopic fractures. Additionally, owing to its lower stiffness, biotite experiences greater deformation, resulting in wider cracks that facilitate the formation of macroscopic fractures. In the 5 % biotite content model (Fig. 16a), the black circles indicate macroscopic fractures that traverse two adjacent biotite minerals, resulting in vertical macroscopic cracks. In contrast, in the 10 % biotite content model (Fig. 16b), four adjacent biotite minerals are arranged at an inclined angle, leading to a transition from vertical to inclined propagation of macroscopic fractures. Furthermore, in the 30 %

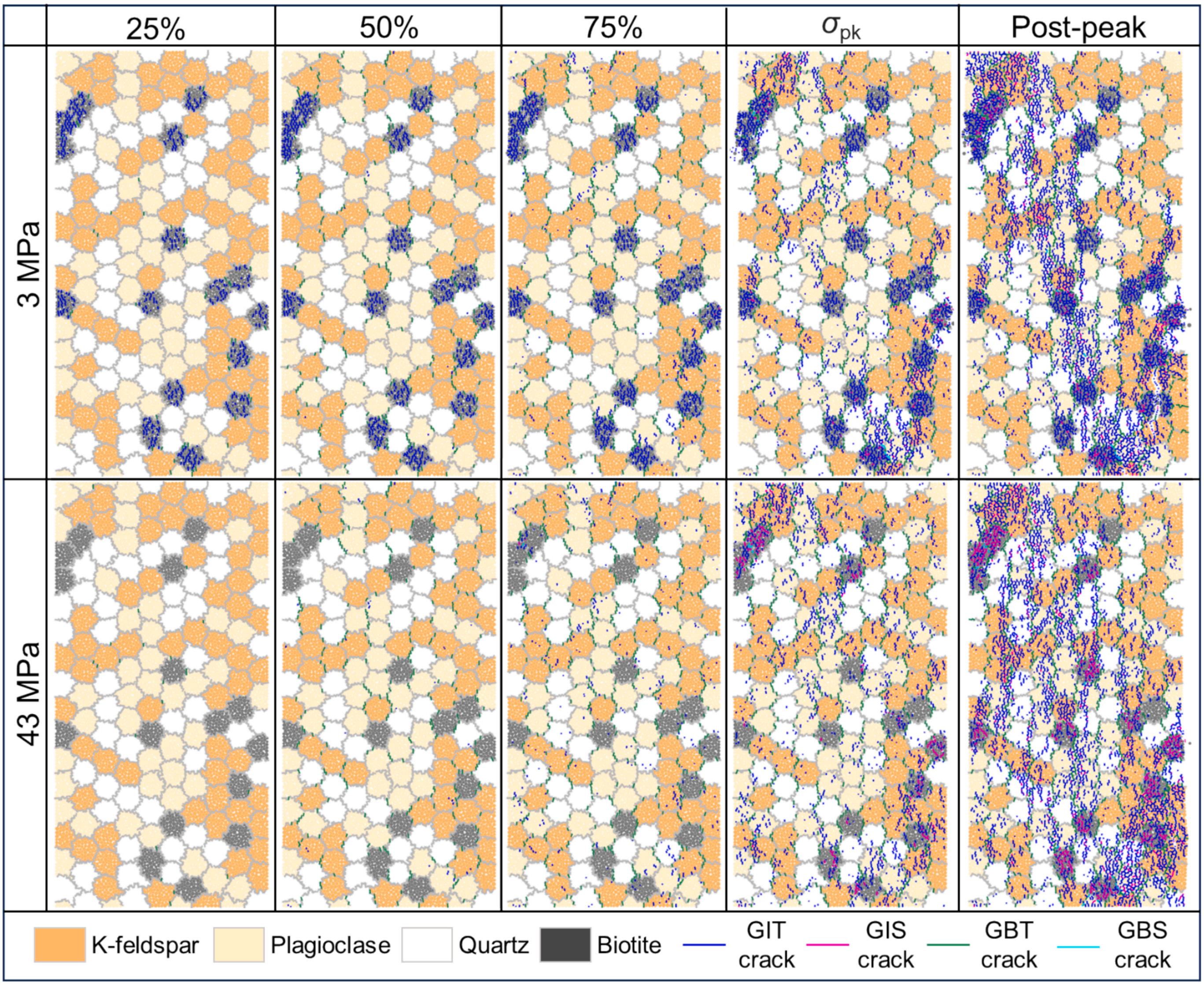

Fig. 20. Crack distribution results for different biotite tensile strengths (3 MPa and 43 MPa) at different stages of the uniaxial compression test. *GB: Grain boundary; GI: Intra-grain; T: Tensile; S: Shear.

biotite content granite model (Fig. 16e), increased density of biotite at its lower section results in nearly all macroscopic fractures being concentrated in this region.

The distribution of cracks for varying biotite content under direct tensile testing is presented in Fig. 17. Tensile cracks predominantly occur along the boundaries of the biotite due to its lower strength. During crack propagation, tensile cracks at non-adjacent biotite boundaries can connect and form macroscopic fractures, while IG tensile cracking is minimal. In the model with 30 % biotite content (Fig. 17e), due to the horizontally adjacent arrangement of biotite grains, tensile cracks propagate and penetrate along grain boundaries to create macroscopic horizontal fractures. Consequently, TS is significantly diminished by the presence of biotite.

Crack ratios in the models with varying biotite content and following uniaxial compressive failure are illustrated in Fig. 18. The effect of biotite content on the ratios of tensile to shear cracks, as well as GI to GB cracks, is minimal. Tensile cracks constitute ~90 % of the total crack numbers, while GI cracks account for ~92 %. This indicates that under uniaxial compression, most minerals exhibit tensile transgranular fracturing, congruent with the experimental observations. As biotite content increases from 5 % to 30 %, the proportion of biotite cracks relative to total cracks rises linearly from 13.3 % to 51.3 %.

3.2. Biotite strength

To examine the effect of biotite strength on the macroscopic mechanical properties of granite, a granite model with 10 % biotite content was utilized as the reference case, based on Section 3.1. Biotite tensile strength parameters of 3 MPa, 13 MPa, 23 MPa, 33 MPa, and 43 MPa were assigned to evaluate impact. The stress–strain curves for models with varying biotite tensile strengths are presented in Fig. 19a and b. The results indicate that as the strength increases, the compressive elastic modulus remains largely unaffected; however, for a strength of 3 MPa, there is a significant reduction in tensile elastic modulus while other conditions show minimal impact. Both UCS and TS of the model increase with increasing biotite strength; notably, post-peak brittle characteristics are not pronounced under both loading conditions when the parameter is 3 MPa.

As illustrated in Fig. 19c and d, the tensile strength of the mineral biotite significantly influences the macroscopic strength of the rock aggregate. With an increase in biotite strength, both UCS and TS rise monotonically; however, their growth rates differ. Following an initial increase from 3 MPa to 13 MPa, there is a marked enhancement in both UCS and TS. In contrast, during the subsequent increment from 13 MPa to 43 MPa, the UCS increases gradually and linearly, while TS exhibits a

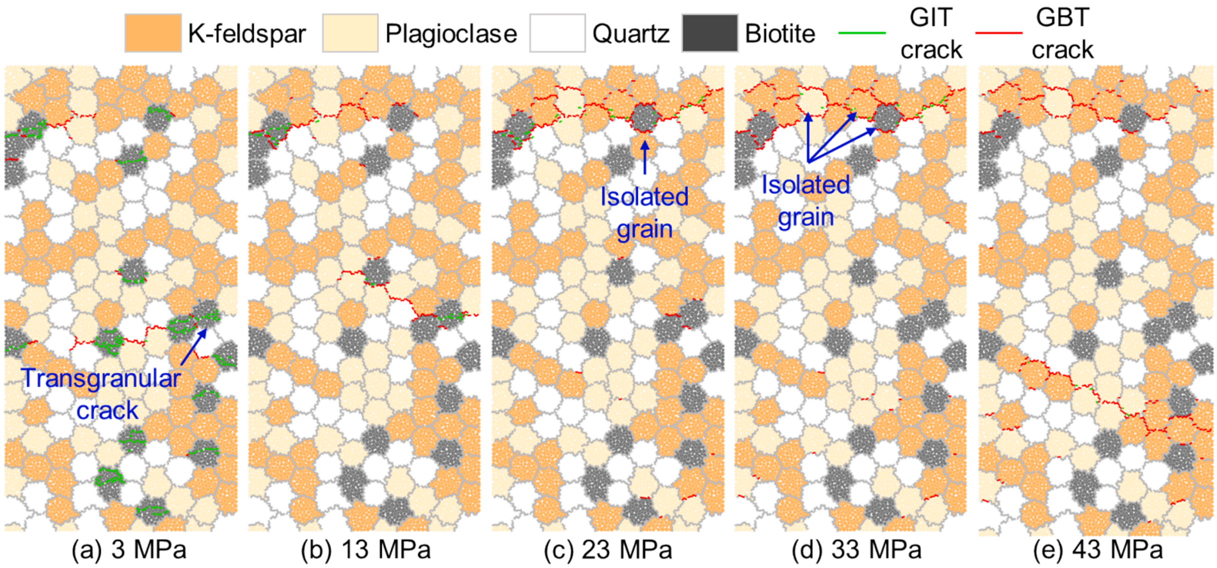

Fig. 21. Crack distribution results for different biotite tensile strength models under the tensile loading. *GB: Grain boundary; GI: Intra-grain; T: Tensile.

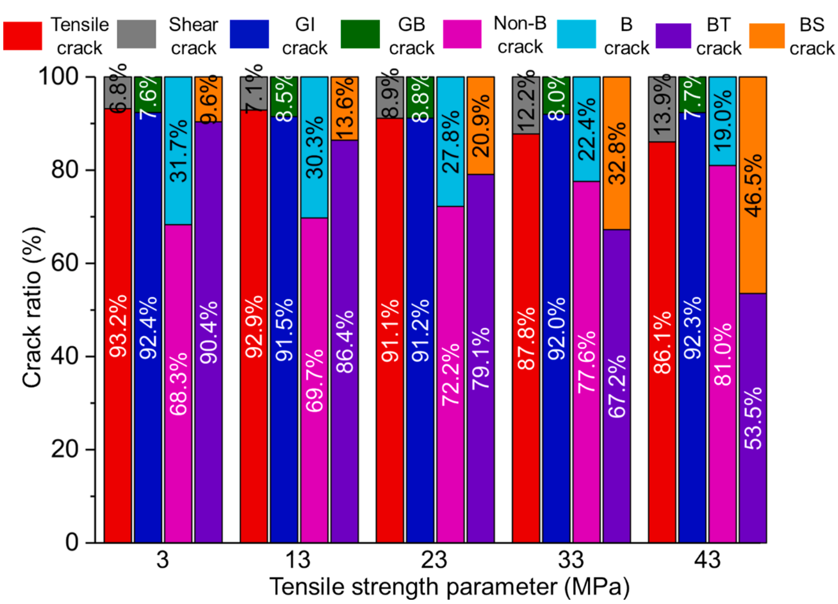

Fig. 22. Crack ratio results for different biotite tensile strengths under uniaxial compression. *GB: Grain boundary; GI: Intra-grain; B: Biotite; T: Tensile; S: Shear.

parabolic growth pattern; notably, between parameters of 33 MPa and 43 MPa, there is minimal change in TS, only increasing by 0.1 MPa. The UCS/TS strength ratio experiences a sharp decline after transitioning from 3 MPa to 13 MPa; however, changes become negligible as it progresses from 23 MPa to 43 MPa before stabilizing at ~20.4. Additionally, σ_{ci} is influenced by tensile strength: following its increase from 3 MPa to 13 MPa, there is a significant rise in σ_{ci} that diminishes; specifically, the σ_{ci}/σ_{pk} ratio increases from 7.94 % to 26.39 % with an increase in mineral strength from 3 MPa to 13 MPa; but only rises 2.81 % when increasing from 23 MPa to 43 MPa.

An analysis of the influence of biotite tensile strength on rock strength indicates that when the tensile strength of biotite is low, there is a pronounced heterogeneity in intensity among minerals, and an increase in biotite tensile strength significantly affects the macroscopic strength of rocks. Conversely, when the tensile strength of biotite becomes high, the difference between strength of biotite and other minerals, such as quartz diminishes, resulting in a reduced impact of increased biotite tensile strength on the macroscopic rock strength.

As illustrated in Fig. 20, the distribution of cracks at various loading stages under biotite tensile strengths of 3 MPa and 43 MPa was analyzed. At 25 % of σ_{pk}, the initiation time and location of cracks are influenced by the biotite tensile strength. When the biotite tensile strength is 3 MPa, a substantial number of tensile cracks form within the biotite grains; conversely, at a tensile strength of 43 MPa, only a limited number of tensile cracks appear at grain boundaries (not restricted to biotite). At 50 % of σ_{pk}, the quantity of GB tensile cracks begins to increase and propagate along grain boundaries for both biotite tensile strength; however, no significant cracks develop within other minerals aside from biotite. At 75 % of σ_{pk}, under low biotite tensile strength conditions, the GB tensile cracks begin to penetrate into those within the biotite; whereas under high biotite tensile strength, shear cracks emerge inside the biotite. At σ_{pk}, there is a marked increase in crack numbers, particularly GI cracks, with numerous shear cracks forming within the biotite when high tensile strength. In the post-peak stage, macroscopic tensile fracturing occurs; with low strength conditions leading to extensive breakage in the biotite accompanied by numerous GI tensile cracks.

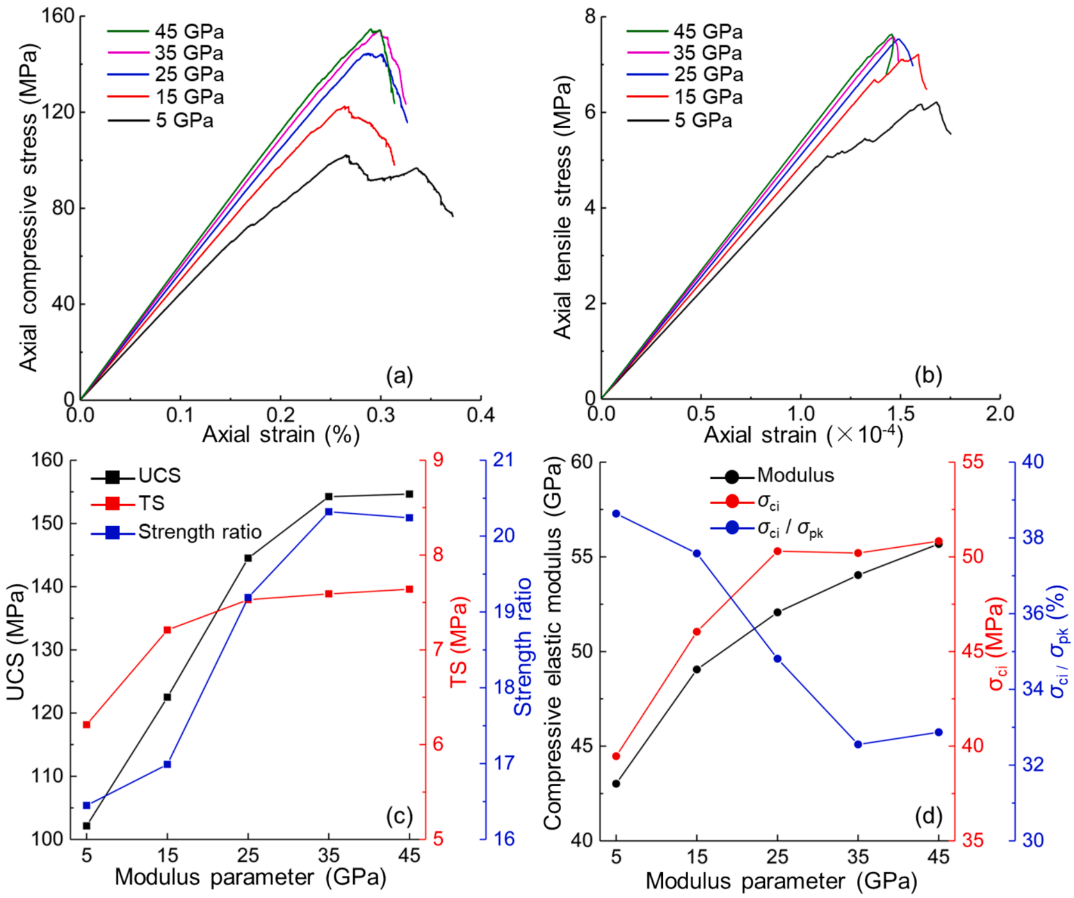

Fig. 23. Influence of modulus of biotite on the macroscopic mechanical properties: (a) Uniaxial compression stress–strain curves; (b) Tensile stress–strain curves; (c) Strength; (d) Characteristic stress.

Conversely, high strength models predominantly yield shear cracks within the biotite. In conclusion, biotite significantly influences both macroscopic and microscopic failure modes and morphologies in rock structures.

As illustrated in Fig. 21, the crack density for granite models with varying tensile strengths for biotite under direct tensile testing was analyzed. Tensile cracks predominantly occur at the grain boundaries; however, due to the lower tensile strength of biotite at 3 MPa, nearly all biotite grains experienced transgranular tensile failure (Fig. 21b). With an increase in the tensile strength of biotite, the tensile resistance improves. Consequently, as these cracks connect and penetrate between the biotite grain boundaries, additional tensile cracks develop around the biotite grains (Fig. 21d), resulting in a completely “isolated grains”.

The crack ratios in models with varying biotite tensile strengths following uniaxial compressive failure are illustrated in Fig. 22. The ratio of tensile cracks exhibits a slight decrease as the tensile strength increases, from 93.2 % to 86.1 %. Conversely, the ratio of GI cracks remains relatively stable at approximately 92 %. The influence of tensile strength on both the ratio of biotite and non-biotite cracks is clear; the ratio of biotite cracks diminishes from 31.7 % to 19.0 % with increasing tensile strength. Additionally, the ratios of shear and tensile cracks within biotite are notably impacted by its tensile strength, decreasing from 90.4 % to 53.5 % as the strength rises. These findings indicate that despite the minor proportion of biotite minerals, their mechanical properties exert a substantial effect on the crack distribution within crystalline rocks.

3.3. Biotite modulus

To examine the impact of biotite stiffness on the macroscopic mechanical properties of granite, a model containing 10 % biotite was chosen as the reference model. The elastic modulus of the biotite grains was assigned five distinct values: 5 GPa; 15 GPa; 25 GPa; 35 GPa; and 45 GPa. The stress–strain curves for the granite models with varying biotite stiffness under uniaxial compression and direct tension tests are presented in Fig. 23a and b. Both the UCS and TS of the model exhibited an increase corresponding to higher biotite stiffnesses. Notably, when the elastic modulus for biotite was set at 5 GPa, the brittle characteristics of the model were not pronounced under either loading condition.

As illustrated in Fig. 23c, the biotite stiffness significantly influences the strength of rock. With an increase in the elastic modulus, both the UCS and TS of the rock exhibit a corresponding increase; however, their growth rates differ. When increasing the parameter from 5 GPa to 25 GPa, the UCS shows nearly linear growth; conversely, during subsequent increments beyond this range, its rate of increase slows and stabilizes. The TS demonstrates a parabolic growth, rising by 1 MPa between 5 GPa and 15 GPa before stabilizing at ~7.5 MPa. Additionally, the UCS/TS strength ratio increases from 16.45 to 20.32 as the modulus increases from 5 GPa to 35 GPa but subsequently decreases to 20.24 when further increased to 45 GPa.

As illustrated in Fig. 23d, the biotite stiffness significantly influences the compressive modulus and σ_{ci} of the rock. Initially, as biotite stiffness increases, the compressive modulus rises rapidly before stabilizing. Similarly, σ_{ci} increases followed by stabilization. The σ_{ci}/σ_{pk} ratio decreases progressively as the parameter increases from 5 GPa to 35 GPa; conversely, it exhibits a slight increase when transitioning from 35 GPa to 45 GPa. These findings suggest that within the range 5–25 GPa, both the compressive modulus and σ_{ci} are particularly sensitive to variations in biotite stiffness.

Fig. 24 illustrates the distribution of microcracks at various loading

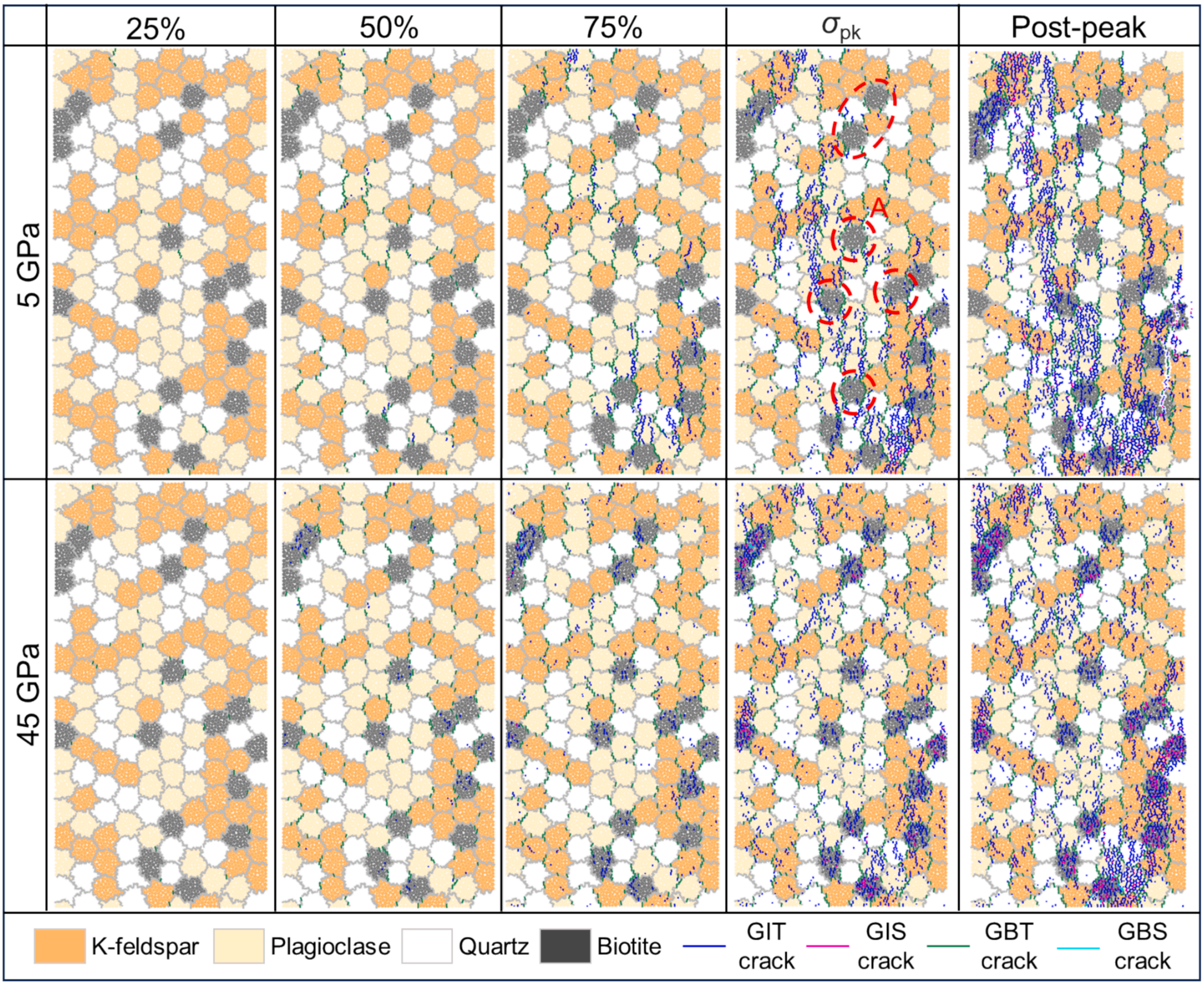

Fig. 24. Crack distributions for different biotite modulus models (5 GPa and 45 GPa) at different stages of uniaxial compression. *GB: Grain boundary; GI: Intragrain; T: Tensile; S: Shear.

stages for biotite with elastic moduli of 5 GPa and 45 GPa. In scenarios involving low biotite stiffness (5 GPa), at an axial stress level of 25 % of the σ_{pk}, only a limited number of tensile cracks are observed at the grain boundaries. As the axial stress reaches 50 % of the σ_{pk}, there is a notable increase in both the quantity and random distribution of GB tensile cracks. In some non-biotite mineral boundaries, some cracks have connected, leading to the formation of GI tensile cracks within non-biotite minerals. When axial stress attains 75 % of σ_{pk}, there is a significant rise in GI tensile crack density within non-biotite minerals. This contrasts sharply with observations from low-strength biotite where more GI tensile cracks are present. Following attainment of σ_{pk} by axial stress, the crack number accelerates significantly; numerous GI shear microcracks initiate within non-biotite minerals, resulting in macroscopic fractures. Notably, as indicated by the red rectangle in the figure, nearly no microcracks develop within biotite grains themselves; instead, existing microcracks propagate through biotite boundaries. Once these microcracks enter into post-peak conditions, they expand rapidly while additional shear cracks emerge inside non- biotite minerals. Macroscopic fractures preferentially extend towards areas rich in biotite aggregates; however, many microcracks either cease propagation or circumvent biotite grains during their propagation process to form " isolated grains".

In scenarios involving high biotite stiffness (45 GPa), the deformation of the biotite is correspondingly diminished. Because the strength of biotite is lower than that of other minerals, biotite has a higher probability of microcrack formation during loading, with tensile cracks initiating and propagating from within the biotite, ultimately resulting in the development of macroscopic fractures that lead to tensile cleavage failure in the model. In conclusion, when biotite exhibits low stiffness, it significantly influences both the initiation and propagation of microcracks while governing macroscopic failure behavior. As the stiffness disparity between minerals diminishes, this influence gradually attenuates.

Fig. 25 illustrates the results of direct tensile tests conducted on granite models with varying biotite stiffness. Crack formation occurs at the grain boundaries; however, at a stiffness of 45 GPa, tensile cracks penetrate through the biotite grains, resulting in transgranular fractures. Conversely, at 5 GPa, most cracks initiate from the biotite and propagate outward along the boundaries of non-biotite minerals. The tensile cracks highlighted within the black frame (Fig. 25) originate from biotite grains and propagate radially before intersecting and connecting with cracks initiated by other biotite grains. Additionally, shear cracks are observed within the biotite grains.

Crack ratios in models with varying biotite modulus following failure

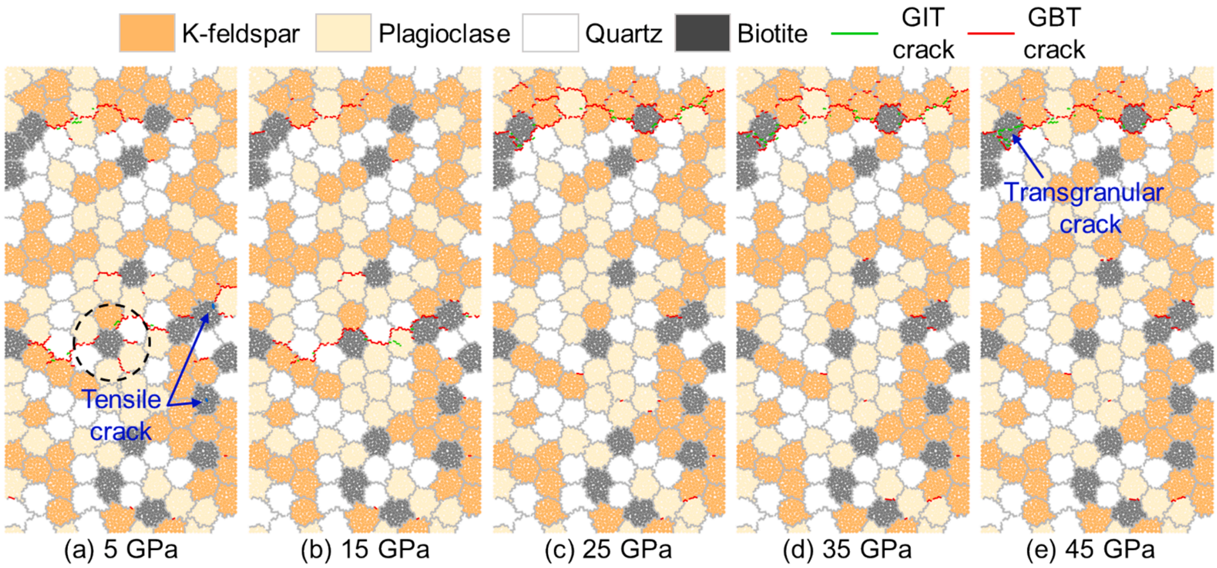

Fig. 25. Crack distributions for different biotite modulus models under extension. *GB: Grain boundary; GI: Intra-grain; T: Tensile.

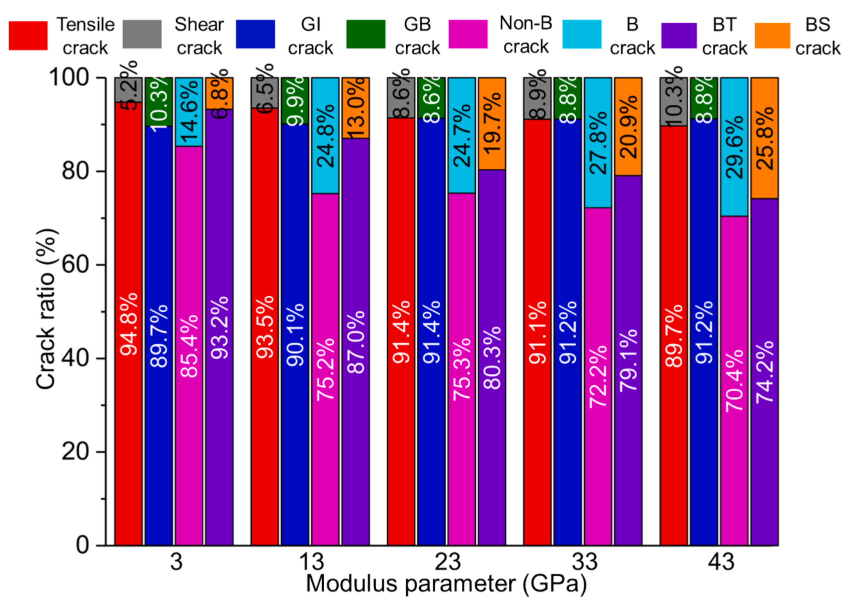

Fig. 26. Crack ratio results for different biotite modulus models under uniaxial compression. *GB: Grain boundary; GI: Intra-grain; B: Biotite; T: Tensile; S: Shear.

in uniaxial compression is illustrated in Fig. 26. In all models examined, the cracks are predominantly tensile; however, their proportion exhibits a slight decrease as biotite stiffness increases, decreasing from 94.8 % to 89.7 %. Conversely, the proportion of GI cracks remains relatively stable. Biotite stiffness significantly influences the ratio of cracks within both biotite and non-biotite minerals. As biotite stiffness increases, the proportion of cracks within biotite rise from 14.6 % to 29.6 %, thereby narrowing the disparity with non-biotite crack counts. Additionally, shear-tension crack proportions within the biotite are notably affected by its stiffness; specifically, as elastic modulus increases, the proportion of tensile cracks within the biotite diminishes from 93.2 % to 74.2 %. These findings indicate that despite its minor content in crystalline rocks, the mechanical properties of biotite minerals exert a substantial influence on the overall distribution of cracks.

4. Influence of mineral grain anisotropy on mechanical and microcracking behavior

GBM models are constrained by their generation methodology (Voronoi tessellation), which precludes the consideration of mineral grain shape and orientation, both of which exhibit anisotropic characteristics. We employ the "templated" – "grain growth" method proposed in this study to regulate the shape and orientation of mineral grains by adjusting the aspect ratio and orientation of the local coordinate system.

We present a series of uniaxial compression and direct tensile tests conducted on granite models characterized by four distinct aspect ratios and five varying rotation angles, aiming to elucidate the effects of mineral grain shape and orientation anisotropy on the mechanical properties and failure mechanisms of granite.

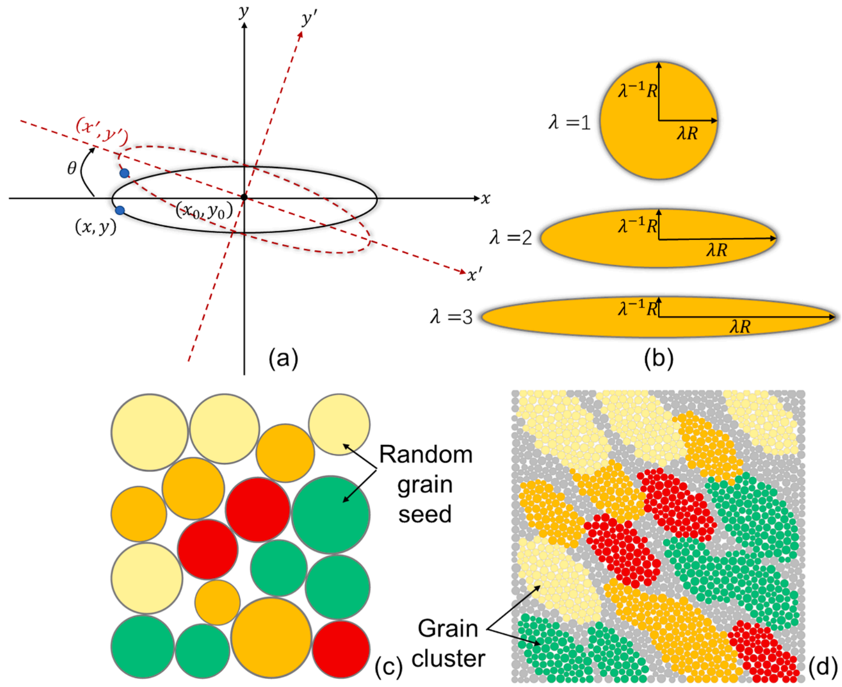

Fig. 27. Schematic diagram of the construction of granite GTM with varying shapes and orientations utilizing the "templated" – "grain growth" method: (a) Defining mineral orientations through coordinate system transformation; (b) Determining mineral shapes based on aspect ratio; (c) Employing random grain seeds; (d) Obtaining mineral grains via grain cluster templated.

4.1. Modeling of granite with different mineral grain shapes and orientations

Fig. 27a and b illustrate schematic representations of the construction of granite GTM models with varying shapes and orientations through the "templated" – "grain growth" method. Each grain cluster is conceptualized as an ellipse, with its area corresponding to that of the grain seed. During the process of grain cluster templated, the center of each grain cluster coincides with that of its respective grain seed, while the orientation is defined by a rotation of the coordinate system; additionally, the shape is characterized by a reduction coefficient applied to the major and minor axes of the ellipse. For instance, if a grain cluster's center is positioned at (x_0, y_0) and it undergoes a rotation angle θ about its centroid, then for a sub-grain located at (x, y) in the original coordinate system, its coordinates in the rotated frame are represented as (x', y'), which can be expressed through a specific transformation relationship:

$$\begin{cases} x' = (x - x_0)\cos(\theta) - (y - y_0)\sin(\theta) + x_0 \\ y' = (x - x_0)\sin(\theta) + (y - y_0)\cos(\theta) + y_0 \end{cases} \tag{2}$$

As illustrated in Fig. 27c and d, let us assume that the major and minor axes of the ellipse are denoted as a and b, respectively. When the point (x', y') satisfies Eq.2, the sub-grain will be classified as belonging to the corresponding grain seed group. The radius of each grain seed is assumed to be R, while λ represents the reduction coefficient applied to the major and minor axes of the ellipse:

$$\begin{cases} \dfrac{(x' - x_0)^2}{a^2} + \dfrac{(y' - y_0)^2}{b^2} \leqslant 1 \\ a = \lambda R, b = \lambda^{-1} R \end{cases} \tag{3}$$

Following the completion of elliptical grain cluster templated, the "gap particles" between grain clusters are classified into mineral groups utilizing the "grain growth" method, thereby yielding granite GTM models with diverse shapes and orientations.

Utilizing the granite model with a biotite content of 10 %, Fig. 28a–d presents various granite models exhibiting mineral grain shapes at different orientations for rotation angles of 0°, 22.5°, 45°, and 67.5° with λ set to values of 1/2/3/4. Conversely, Fig. 28e–i illustrate granite models featuring distinct mineral grain orientations at rotation angles of 0°/22.5°/45°/90° while maintaining $\lambda = 3$.

4.2. Mineral grain shapes

The shape of mineral grains is characterized by λ. When λ exceeds 1, the grain clusters transition from a circular to an elliptical form, resulting in geometric anisotropy. Assuming uniform orientation of grain clusters across all models, granite models with varying mineral grain shapes are constructed to investigate the influence of grain shape anisotropy on both macroscopic mechanical properties and microscopic cracking characteristics of rocks through analysis of uniaxial compression tests and direct tensile tests.

As illustrated in Fig. 29a and b, the stress–strain curves for granite with varying mineral grain shapes under uniaxial compression and tensile tests are presented. The shape of mineral grains significantly influences the strength and elastic modulus of rocks. Fig. 29c and d further elucidates the impact of mineral grain shape on the macroscopic mechanical properties of rocks. Specifically, as depicted in Fig. 29a, when λ increases from 1 to 2, the UCS decreases from 154.24 MPa to 145.66 MPa; subsequently, it gradually rises from 145.66 MPa to 156.39 MPa as λ progresses from 2 to 4. This variation can be attributed to changes in the shape of mineral grains affecting the model's compressive performance: at $\lambda = 1$, mineral grains approximate hexagonal packing, whereas at $\lambda = 2$, they adopt a rhombic configuration—resulting in inferior compressive performance compared to hexagonal packing due to spatial arrangement factors. When λ reaches values of 3 and 4, the mineral grain shape becomes flattened oval, leading to more horizontal grain boundaries; since boundary strength is inherently weaker than that of individual grains, this results in greater pressure being borne by these minerals during compression and consequently enhances the model's compressive performance overall. Conversely, TS exhibits a gradual decline with increasing λ.

As λ increases from 1 to 2, the TS of the model experiences a

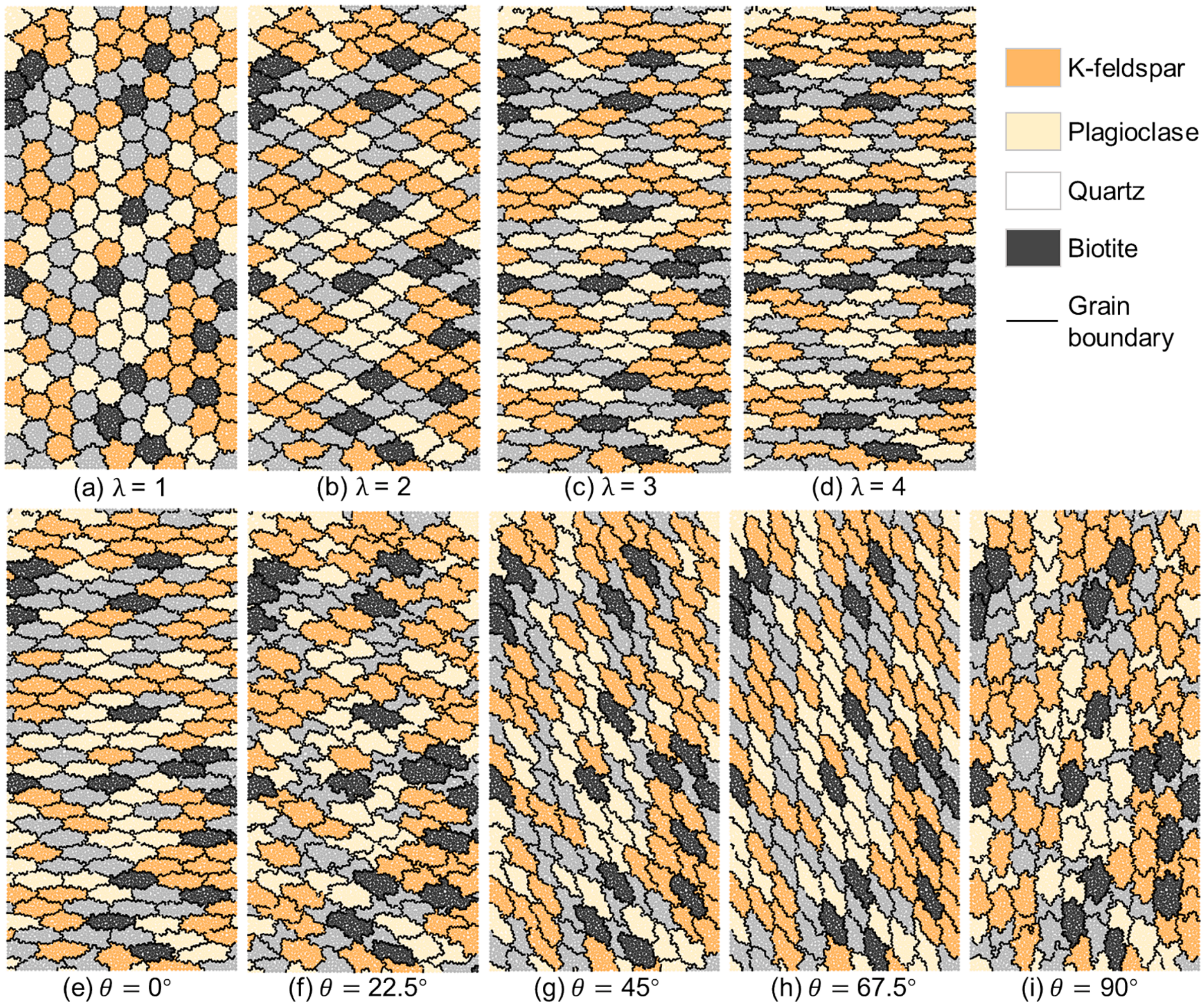

Fig. 28. Granite models characterized by diverse mineral grain shapes and orientations.

significant reduction; however, this decline in TS diminishes as λ progresses from 2 to 4. This phenomenon can be attributed to the fact that with increasing λ, the mineral grain shape becomes increasingly flattened, making horizontal mineral boundaries more susceptible to tensile failure. Additionally, the UCS-TS strength ratio of the model exhibits an almost linear increase with rising values of λ.

Fig. 29d illustrates the impact of variations in mineral grain shape on the compressive modulus and σ_{ci} of rocks. The compressive modulus exhibits a gradual increase as the λ rises. Following an increase in λ from 1 to 2, there is a significant enhancement in the compressive modulus; however, this rate of increase diminishes as λ progresses from 2 to 4. The trend observed for σ_{ci} mirrors that of the compressive modulus: after λ increases from 1 to 2, the rise in fracture stress is more pronounced, followed by a deceleration in its growth; additionally, the ratio of σ_{ci} to σ_{pk} is approximately 32.55 % at $\lambda = 1$ and increases to around 39 % within the range of λ values from 2 to 4.

As illustrated in Fig. 30, the results of uniaxial compression tests on granite models with varying mineral grain shapes indicate that the shape of mineral grains exerts minimal influence on the macroscopic failure characteristics of rocks. In all four cases, rock failure occurs via tensile cleavage, with the majority of microcracks being vertical and aligned parallel to the loading direction. Shear microcracks are predominantly observed within the biotite grains.

Fig. 31 illustrates that the shape of mineral grains exerts a slight influence on the ratio of various microcracks within the model subjected to uniaxial compressive loading, with tensile cracks constituting approximately 90 % of the total crack. Alterations in mineral grain shape result in changes to the orientation of boundary contacts. As λ increases, mineral grains become increasingly flattened, leading to a reduction in the number of vertical boundary contacts. Under uniaxial loading conditions, most boundary tensile cracks are aligned parallel to the loading direction (vertical), resulting in a decrease in the ratio of boundary tensile cracks as λ rises.

As illustrated in Fig. 32, the results of the direct tensile test conducted on granite models with varying mineral grain shapes are presented. By integrating the trend of TS variation observed in Fig. 29b, it is evident that the shape of mineral grains significantly influences TS. As λ increases, a greater number of mineral boundary contacts become nearly horizontal; consequently, due to the relatively low strength of these boundaries under direct tensile loading, cracks predominantly propagate horizontally along the mineral boundaries. Therefore, as λ increases, there is an increased likelihood for the model to develop horizontal boundary tensile cracks, leading to a corresponding decrease in TS.

4.3. *Mineral grain orientations*

The orientation of mineral grains is defined by manipulating the rotation angle θ of the local coordinate system. As θ is rotated from 0° to 90°, the elliptical grain cluster transitions gradually from a horizontal to a vertical orientation, resulting in geometric anisotropy within the model. Assuming that all grain clusters in the models maintain an

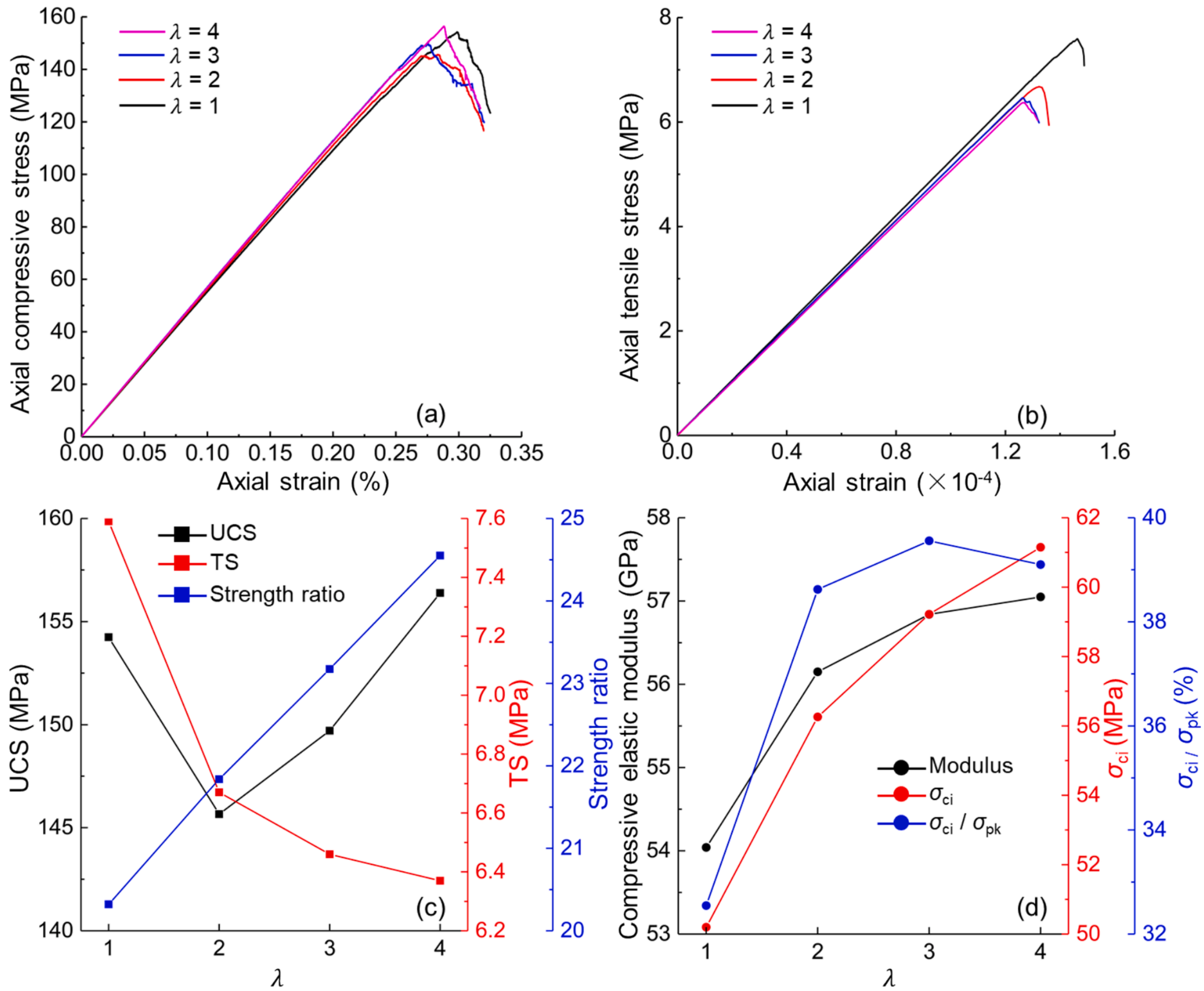

Fig. 29. Influence of mineral grain shapes on the macroscopic mechanical properties: (a) Uniaxial compression test stress–strain curves; (b) Tensile test stress–strain curves; (c) Strength; (d) Modulus and characteristic stress.

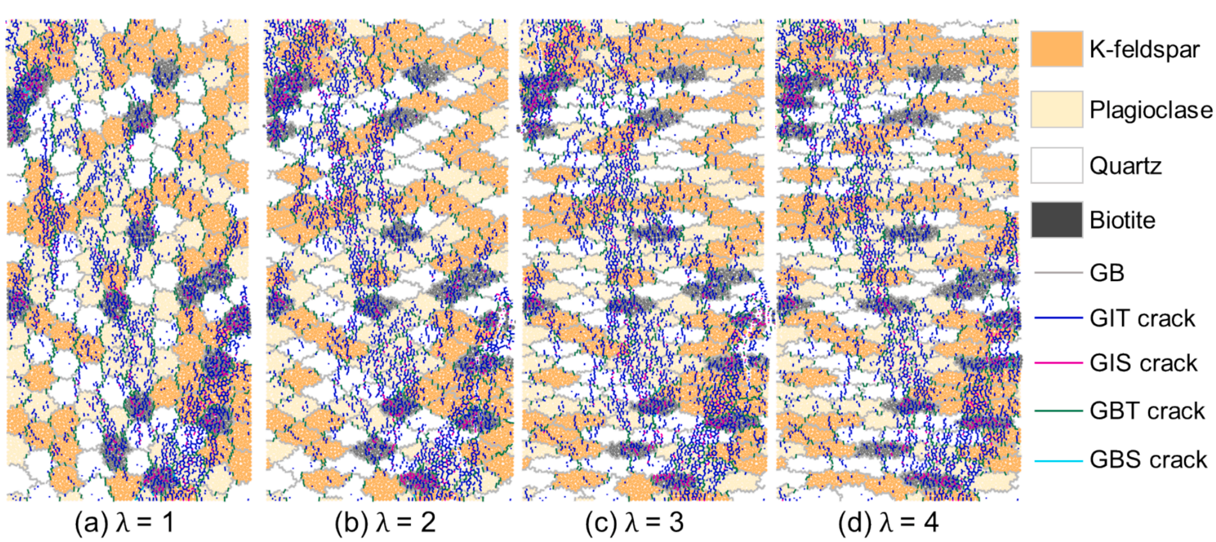

Fig. 30. The crack distribution results of different mineral grain shape models under uniaxial compression. *GB: Grain boundary; GI: Intra-grain; T: Tensile; S: Shear.

identical aspect ratio ($\lambda = 3$), this study investigates how the orientation anisotropy of mineral grains affects both macroscopic mechanical properties and microscopic failure characteristics.

As illustrated in Fig. 33a and b, the stress–strain curves corresponding to various mineral grain orientations in granite during uniaxial compression and tensile tests are presented. The results indicate that the orientation of mineral grains significantly influences the mechanical properties of rocks, including strength and elastic modulus.

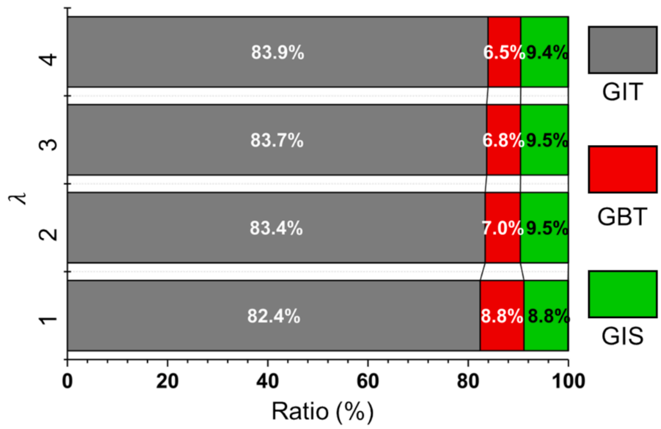

Fig. 31. Ratio of cracks during uniaxial compression loading in granite models with varying mineral grain shapes. *GB: Grain boundary; GI: Intra-grain; T: Tensile; S: Shear.

With an increase of θ, the brittle characteristics observed in the uniaxial compression stress–strain curve gradually diminish. Fig. 33c and d further demonstrates the impact of mineral grain orientation on macroscopic mechanical properties of rocks. As the θ of mineral grains rotates from 0° to 90° within the granite model, there is a gradual decrease in UCS, while TS exhibits a corresponding increase. This phenomenon can be attributed to changes in the orientation of mineral boundary contacts resulting from variations in grain orientation; since both strength and stiffness at these boundaries are lower than those associated with individual grains, their alignment affects microcrack propagation during uniaxial compression and tensile loading, ultimately leading to alterations in macroscopic mechanical properties of the model. Additionally, it is noteworthy that the strength ratio is also significantly influenced by grain orientation; as θ progresses from 0° to 90°, this ratio decreases almost linearly from 23.17 to 14.68.

The compressive modulus of the rock exhibits a gradual decrease as the θ increases. Following the rotation of θ from 0° to 22.5°, there is a significant reduction in the compressive modulus; however, this decline slows down as θ progresses from 22.5° to 90°. The TS decreases gradually with increasing θ, with only a minor reduction observed after θ rotates from 0° to 22.5°. The trend in the strength ratio mirrors that of TS, decreasing from 39.56 % to 31.31 % over the range of θ from 0° to 90°. Analyzing these results indicates that when mineral grain orientation is horizontal, there is a substantial reduction in contact points along the loading direction (vertical) due to mineral boundary orientations being predominantly vertical relative to this loading direction (horizontal). Consequently, both the model's resistance to deformation and its capacity for resisting microcrack initiation are significantly enhanced.

Fig. 34 illustrates the results of the uniaxial compression test conducted on granite models with varying mineral grain orientations, along with the corresponding crack distribution and bubble density diagrams. The results indicate that while all five models exhibit macroscopic tensile failure, the orientation of macroscopic tensile cracks in the central regions differs among them. When the θ is set at 0°, a majority of the cracks align parallel to the loading direction (vertical), resulting in transgranular tensile failures. As θ transitions from 22.5° to 67.5°, there is a notable inclination in the orientation of these macroscopic tensile fractures within the model's center, attributed to alterations in grain boundary contact orientations that influence microcrack propagation directions. With an increase in θ, there is also a corresponding rise in the proportion of grain boundary tensile cracks (depicted as green bubbles). At θ equal to 90°, although again vertical, the orientation of macroscopic tensile cracks reveals an increased incidence of failures along grain boundaries compared to when θ was at 0°.

Fig. 35 illustrates the influence of mineral grain orientation on the ratio of various microcracks within the model subjected to uniaxial compression loading. The alteration in mineral grain orientation results in a corresponding change in the orientation of boundary contacts. As θ increases, the orientation of these boundary contacts transitions gradually from horizontal to vertical, leading to an increase in the number of vertical boundary contacts. Under uniaxial loading conditions, GB tensile cracks predominantly align with the loading direction (vertical); consequently, as θ increases, there is a gradual decrease in the proportion of GI tensile cracks and a concomitant increase in GB tensile cracks.

Fig. 36 illustrates the distribution of cracks observed in the direct

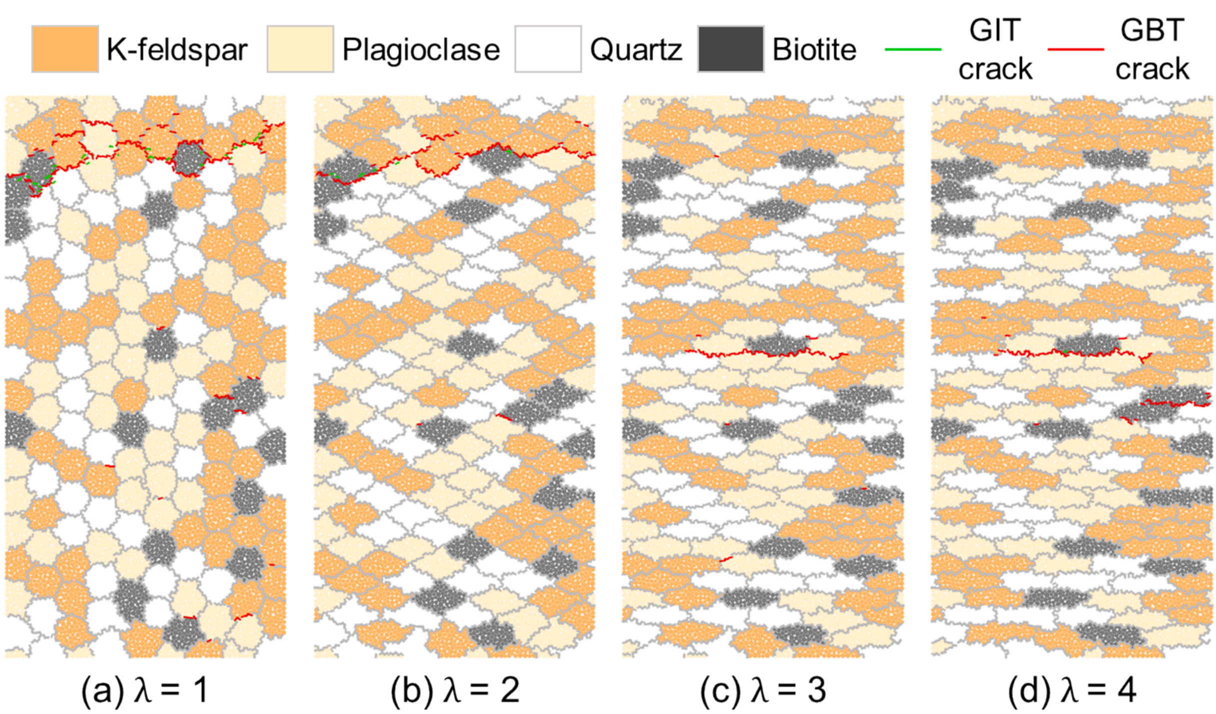

Fig. 32. The crack distribution results of different mineral grain shape models under tensile test. *GB: Grain boundary; GI: Intra-grain; T: Tensile.

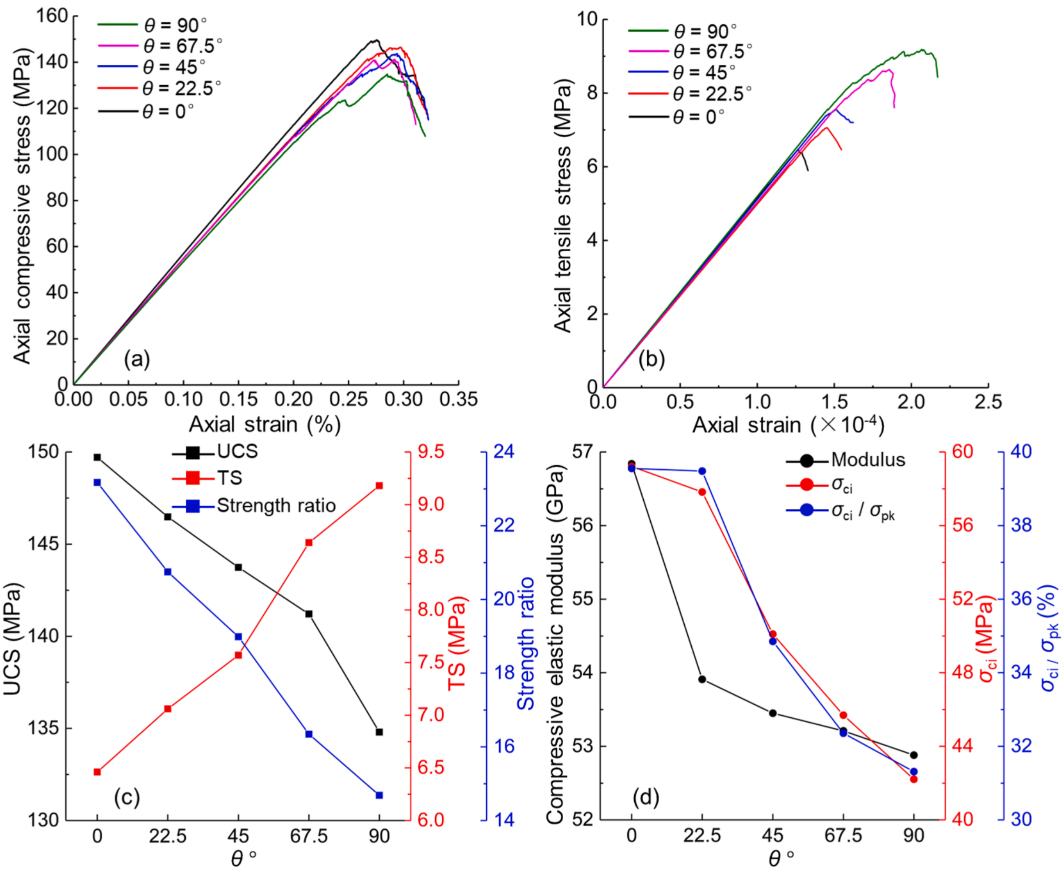

Fig. 33. The influence of mineral grain orientations on the macroscopic mechanical properties: (a) Uniaxial compression test stress–strain curves; (b) Tensile test stress–strain curves; (c) Strength; (d) Modulus and characteristic stress.

tensile test of granite models with varying mineral grain orientations. By correlating this with the trend of TS variation depicted in Fig. 33d, it is evident that mineral grain orientation significantly influences TS. As the θ increases, a greater number of mineral boundary contacts transition from horizontal to vertical alignment. Under direct tensile loading conditions, due to the relatively lower strength of mineral boundaries, cracks predominantly propagate horizontally along these boundaries. At smaller values of θ, the model is more susceptible to forming gb tensile cracks; however, as θ increases, these tensile cracks are increasingly impeded by mineral grains during their horizontal propagation along the boundaries, resulting in more tortuous boundary contacts and reducing the likelihood of tensile failure within the model.

5. Discussion

5.1. Influential mechanisms of biotite on crack propagation behavior

Zhou et al. (2024) and Mahabadi et al. (2014) found through experiments that biotite has a significant influence on the propagation of microcracks. As depicted in Fig. 37, there are two modes of crack propagation around a biotite grain: intergranular propagation and transgranular propagation, which is related to the mechanical and geometric properties of biotite. As shown in Fig. 37c, when the biotite stiffness is 5 GPa, the microcracks propagate around a biotite grain form an “isolated biotite grains”. In Fig. 37f, when the stiffness of mica is 15 GPa, the microcracks around a biotite grain undergo splitting through the biotite grain after transgranular propagation.

Fig. 38a illustrates the distribution of local maximum principal stress surrounding the biotite in circle A, as indicated in Fig. 24, during uniaxial compressive loading at various stages, with biotite elastic moduli set at 5 GPa and 45 GPa respectively. In the initial loading phase (at 25 % and 50 % of σ_{pk}), stress is predominantly concentrated at the mineral boundaries of the biotite in both cases, thereby increasing the likelihood of microcrack formation along these boundaries during this stage. As axial stress continues to escalate, for cases where the biotite modulus is low, the phenomenon of stress concentration begins to extend into adjacent non-biotite minerals; meanwhile, internal stresses within the biotite remain minimal due to its reduced modulus. Conversely, when considering a higher biotite modulus case, changes in the stress field throughout loading are markedly different from those observed with a lower modulus: there exists no significant stress differential between biotite and non-biotite minerals because of the lower strength of biotite; consequently, an extensive stress zone traverses through the interior of the biotite leading to transgranular macroscopic failure.

Fig. 38b illustrates the evolution of force chains in the model for biotite with elastic moduli of 5 GPa and 45 GPa, where color and thickness denote the magnitude of contact forces. In cases involving biotite with lower stiffness, at 50 % of σ_{pk}, contact forces are predominantly concentrated around the biotite grains, while internal contact forces within the biotite remain minimal; this observation elucidates why microcracks primarily develop at the boundaries of the biotite during this stage. At σ_{pk}, the stress differential between mineral boundaries and their interiors diminishes, resulting in some damage occurring within the biotite itself. Conversely, for cases involving higher stiffness biotite, as loading progresses, there is no significant stress difference observed between the boundaries and interior of the biotite.

5.2. Mineral boundary influence

The analysis of the results indicates that variations in grain shape and orientation result in changes to both the number and orientation of mineral boundary contacts, which significantly influence the macro-

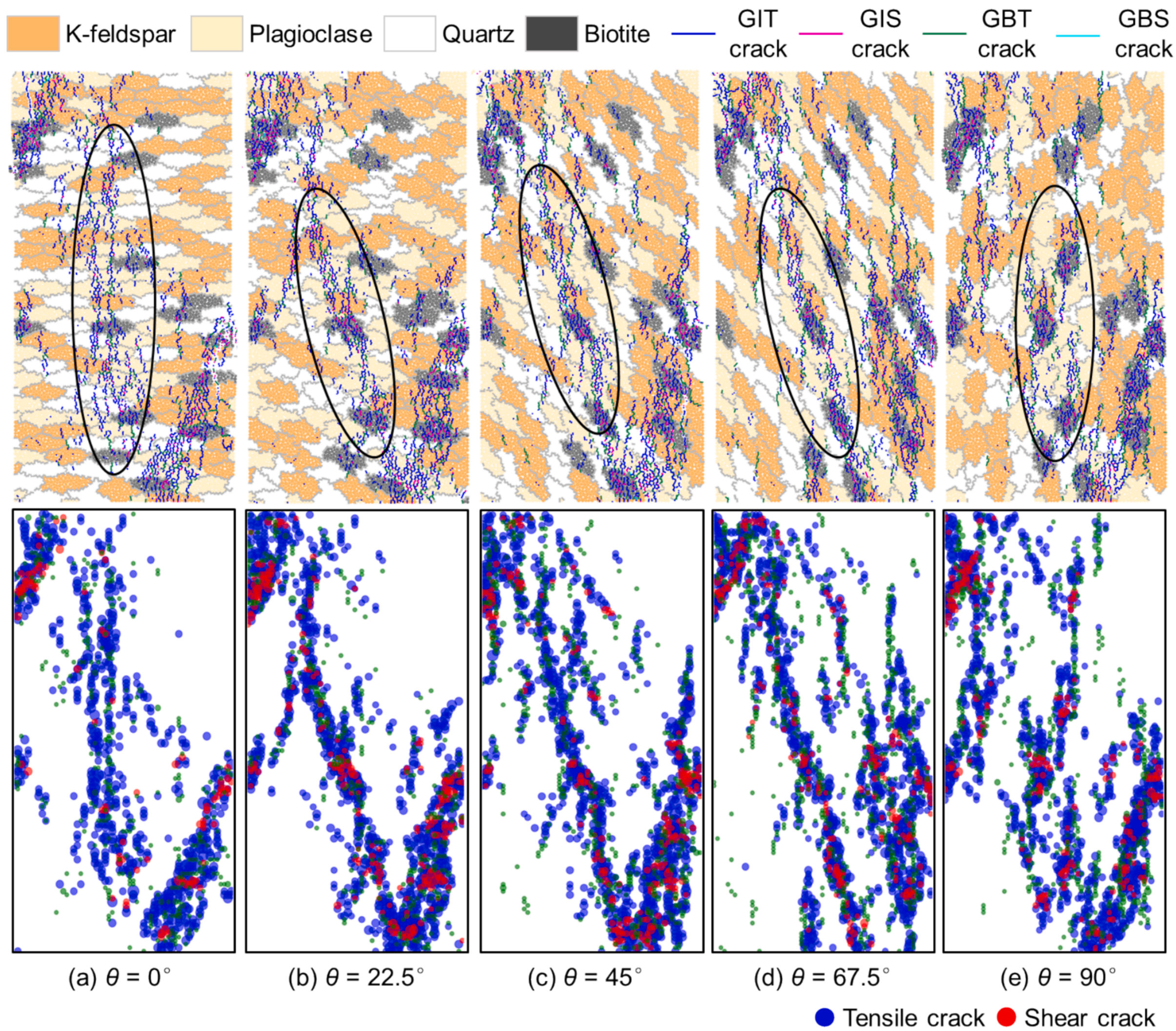

Fig. 34. The crack distribution results of different mineral grain orientation models under uniaxial compression. *GB: Grain boundary; GI: Intra-grain; T: Tensile; S: Shear.

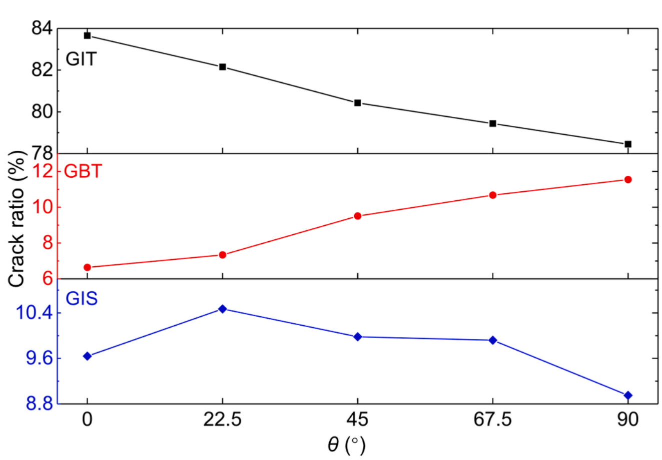

Fig. 35. Ratio of microcracks in granite models subjected to uniaxial compression with varying mineral grain orientations. *GB: Grain boundary; GI: Intra-grain; T: Tensile; S: Shear.

scopic mechanical properties of the granite model. As the λ increases, the mineral grain shape transitions from circular to elliptical. During this transformation, the area of the elliptical grain cluster is maintained equal to that of the grain seed; thus, alterations in grain shape have minimal influence on mineral ratios. However, as λ increases from 1 to 4, there is a corresponding increase in the number of horizontal GB contacts. This phenomenon occurs because when the area of the elliptical grain cluster A_c equals that of its circular counterpart A_p, its circumference C_c exceeds that of circle C_p. Furthermore, as λ increases, C_c becomes increasingly greater than C_p.

$$\begin{cases} a = \lambda R, b = \lambda^{-1} R \\ A_c = \pi R^2, A_p = \pi ab \\ C_c = 2\pi R, C_p = 2\pi b + 4(a-b) \end{cases} \tag{4}$$

$$C_p - C_c = 4\left(\lambda + 1 - \frac{\pi}{2}\right)(\lambda - 1)\frac{R}{\lambda} \tag{5}$$

Consequently, when $\lambda > 1$, it follows that $C_p > C_c$; as λ increases, this indicates a corresponding rise in the number of GB contacts. Fig. 39 illustrates the number of GB contacts across various orientations for different mineral grain shapes. As λ increases, there is an overall increase in total number, with a significant enhancement observed in the number of horizontal contacts.

Fig. 40 illustrates the number of GB contacts across various mineral grain orientations as the θ of the grains varies. A significant number of GB contacts also undergo rotation in tandem with the grains, leading to pronounced anisotropy.

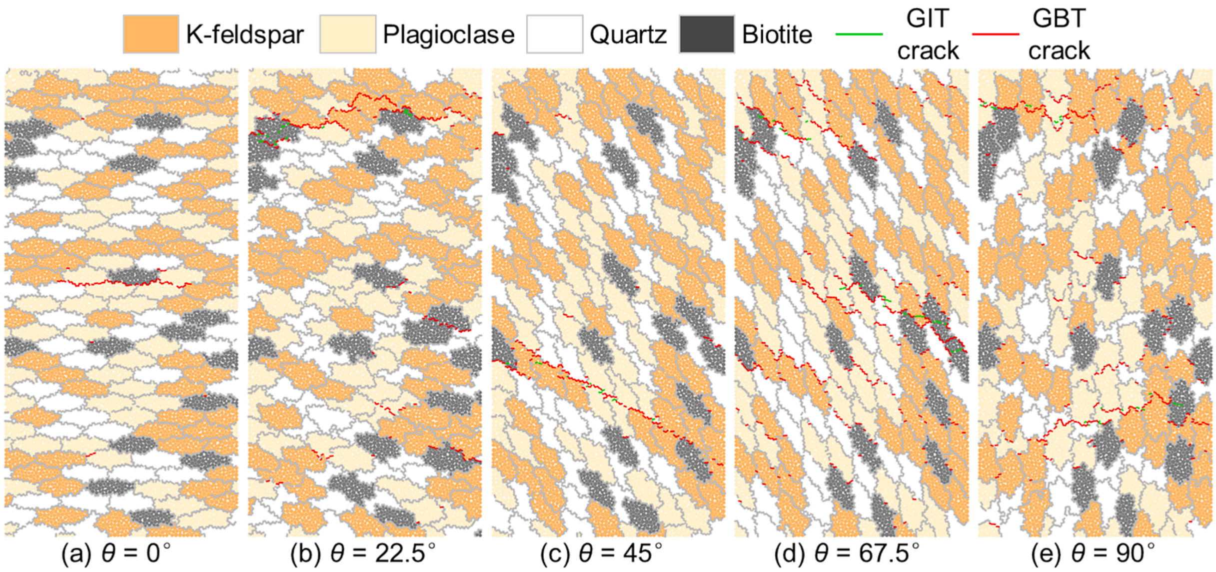

Fig. 36. The crack distribution results of different mineral grain orientation models under the tensile test. *GB: Grain boundary; GI: Intra-grain; T: Tensile.

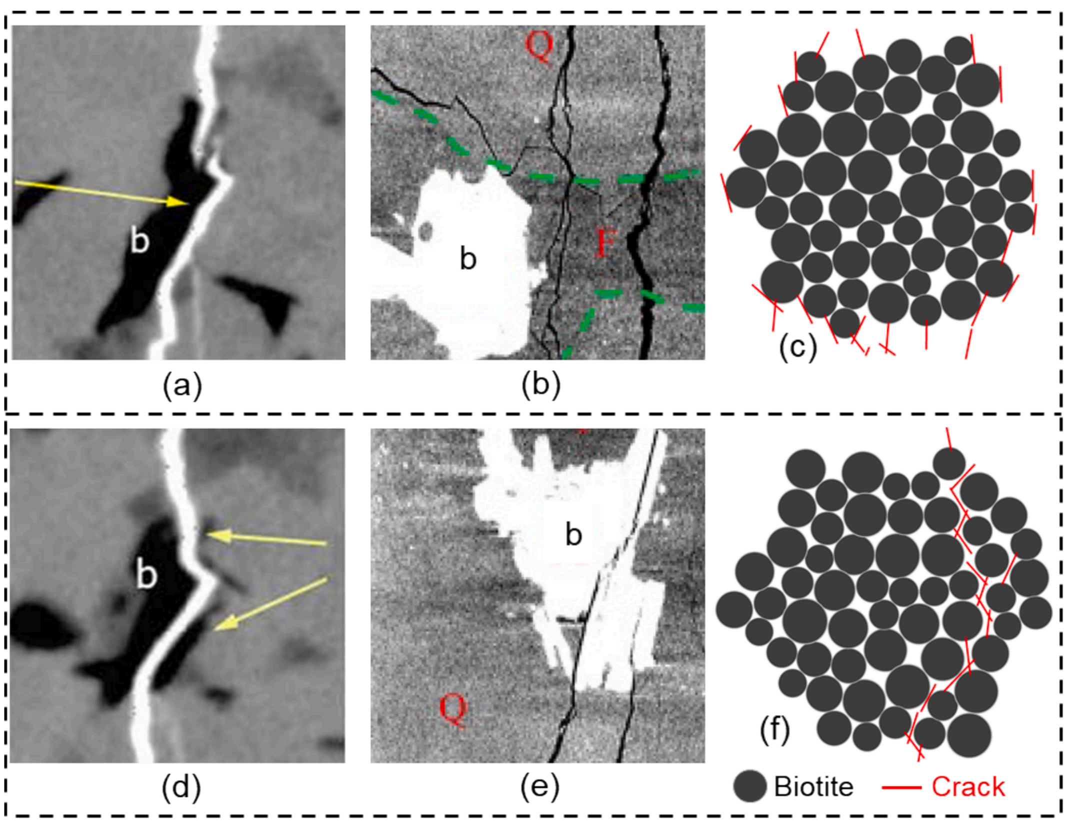

Fig. 37. Comparison of distributions of microcracks around biotite grain obtained from CT scanning (Zhou et al., 2024; Mahabadi et al. 2014) and numerical simulation: (a) – (c) show the intergranular cracking in biotite; (d) – (f) show the transgranular cracking in biotite. *b: biotite; Q: quartz; F: feldspar.

6. Conclusions

This study introduces a novel method for characterizing the microstructural features of granite minerals, referred to as the "templated" – "grain growth" method. Through the development of a grain texture model (GTM) that accurately characterizes the microscopic mineral grain structure of granites, Subsequent comparison with experimental results for validation determine that this novel model effectively captures the macroscopic mechanical properties (including elastic modulus, uniaxial/triaxial compressive strength, tensile strength, strength ratio and brittle-ductile transition) as well as the microcrack propagation processes and macroscopic failure characteristics of granites. Additionally, the study examined how heterogeneity such as biotite content, strength and stiffness influence the mechanical properties and failure behaviors of granite. Furthermore, a novel method was introduced to explore the effects of mineral grain shape and orientation on mechanical properties. The findings offer profound insights into the mechanisms underlying microscopic cracking and failure evolution in crystalline

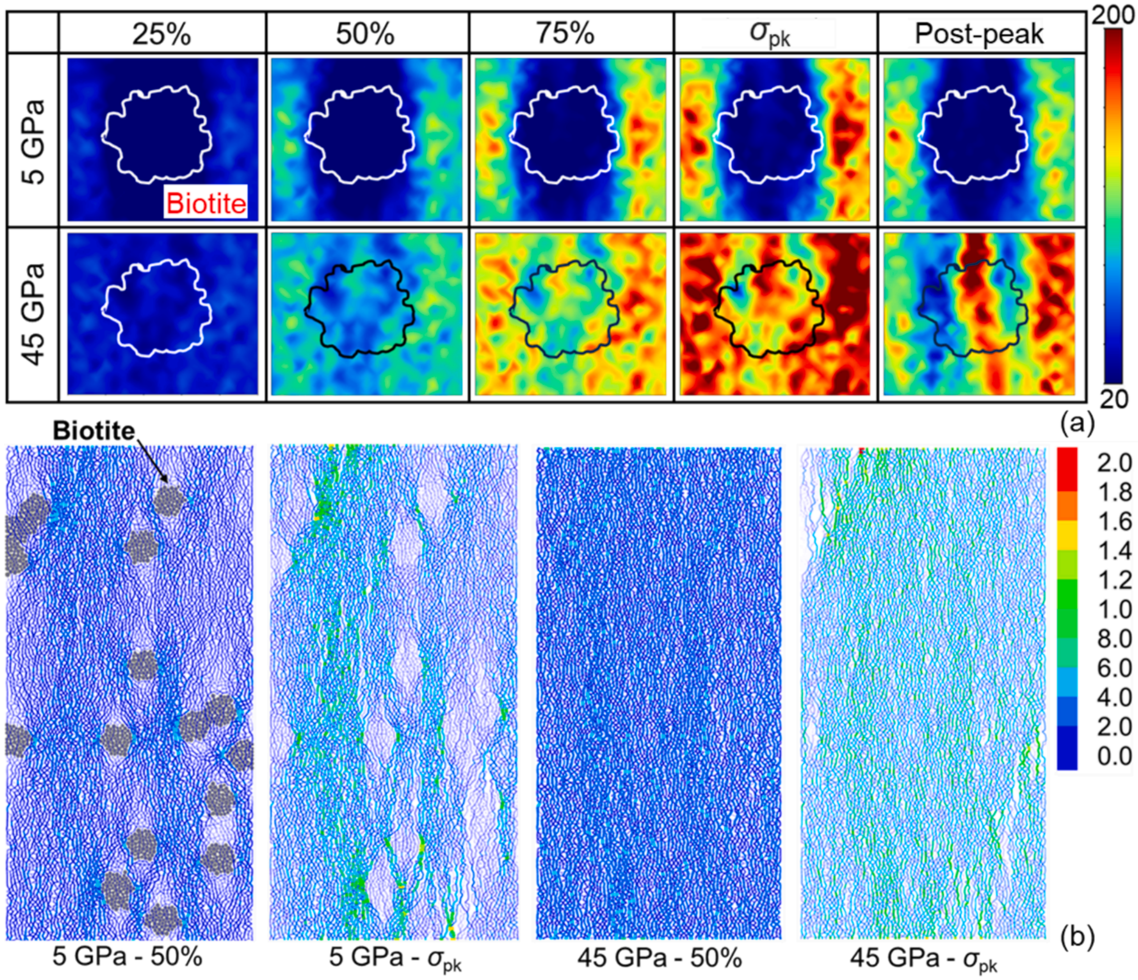

Fig. 38. Variations in stress for different biotite stiffness models during the uniaxial compression process: (a) Maximum principal stress (unit: MPa); (b) Contact force chain (unit: 10^5N).

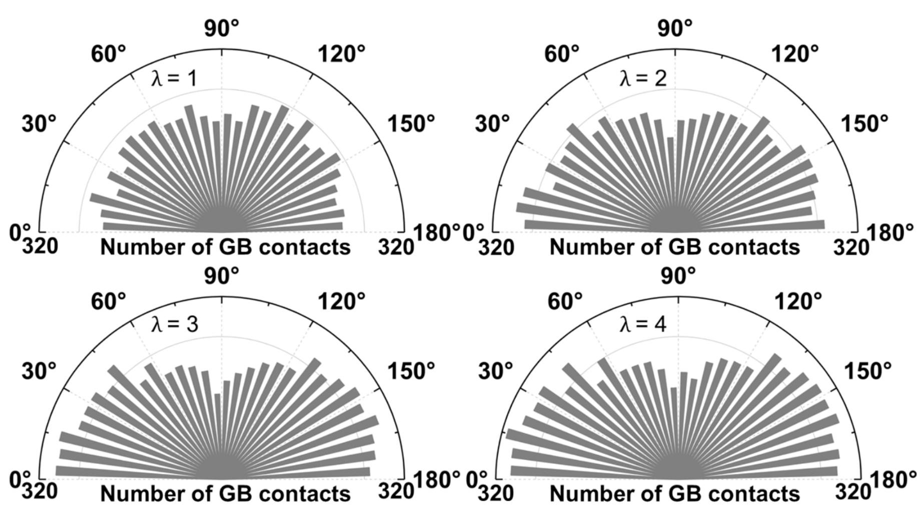

Fig. 39. Rose diagram illustrating the GB contact distribution of various mineral grain shapes model.

rock minerals along with their anisotropic behavior. The principal conclusions drawn from this study are as follows:

(1) Biotite exhibits a pronounced influence on the macroscopic mechanical properties and failure characteristics of granite, attributable to its comparatively lower strength and stiffness relative to other minerals. With the increase in biotite content from 5 % to 30 %, the UCS of the model decreased by 31.2 %, the TS decreased by 21.8 %, and the compressive modulus decreased by 11.9 %. When the tensile strength of the biotite increased from 3 MPa to 43 MPa, the UCS of the model increased by 20.7 %, and the TS increased by 78.3 %. Furthermore, as the elastic modulus

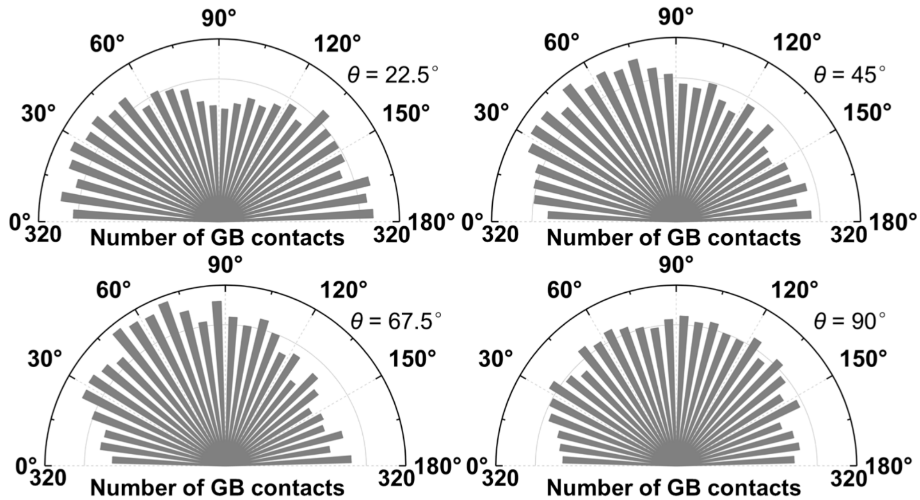

Fig. 40. Rose diagram illustrating the GB contact distribution of various mineral grain orientations model.

of the biotite increased from 5 GPa to 45 GPa, the UCS of the model increased by 51.4 %, the TS increased by 23.1 %, and the compressive modulus increased by 29.4 %.

(2) The effects of biotite strength and stiffness on the propagation of cracks in granite are distinct. A reduction in biotite tensile strength results in an increase in transgranular cracking within the biotite, with these cracks interacting to facilitate the fragmentation of biotite and ultimately resulting in failure. Conversely, as the stiffness of biotite decreases, adjacent minerals are more susceptible to crack formation, while microcracks within biotite minerals diminish. Under uniaxial compression, when microcracks propagate towards the biotite, their paths deviate at low stress due to the relatively lower stiffness of biotite. Subsequently, these cracks will extend along the grain boundaries of the biotite, resulting in the formation of "isolated grains".

(3) The alteration in grain shape results in a variation in the number of GB contacts with differing orientations, thereby influencing the macroscopic mechanical properties of granite. As the reduction coefficient λ increases from 1 to 4, the mineral boundaries become progressively straighter. Consequently, the TS of the model decreases by 16.1 %, the UCS-TS ratio increases by 17.2 %, and the crack propagation along the grain boundaries during tensile tests exhibits a more linear path.

(4) A change in grain orientation induces a corresponding change in the orientation of GB contacts, resulting in pronounced anisotropy that influences the macroscopic mechanical properties of granite. As the rotation angle θ increases from 0° to 90°, the TS of the model increases by 29.6 %, the UCS-TS ratio decreases by 36.6 %. During uniaxial compression and direct tensile loading, the orientation of GB contacts significantly affects microcrack propagation, thereby inducing alterations in the macroscopic mechanical characteristics of the model. At smaller values of θ, the model is more susceptible to GB tensile cracks; however, as θ increases, GB contacts become increasingly curved in the horizontal direction, leading to greater obstruction of tensile cracks by mineral grains during horizontal propagation and rendering the model less likely to experience tensile failure.

CRediT authorship contribution statement

Sui-Feng Wang: Writing – original draft, Software, Methodology, Investigation. **Tao Wang:** Writing – review & editing, Supervision, Resources. **Derek Elsworth:** Writing – review & editing, Supervision. **Xian-Yu Zhao:** Software, Resources, Methodology. **Li-Ping Zhang:** Writing – review & editing, Supervision.

Declaration of competing interest

The authors declare that they have no known competing financial interests or personal relationships that could have appeared to influence the work reported in this paper.

Acknowledgements

This work received support from the China Scholarship Council (CSC, Grant No. 202306270120) and the program of Key Science and Technology Project of Power Construction Corporation of China (No. DJ-ZDXM-2023-03). DE gratefully acknowledges support from the G. Albert Shoemaker endowment.

Data availability

Data will be made available on request.

References

Chen, Y., Nagaya, Y., Ishida, T., 2015. Observations of fractures induced by hydraulic fracturing in anisotropic granite. Rock Mech. Rock Eng. 48 (4), 1455–1461. https://doi.org/10.1007/s00603-015-0727-9.

Geng, P., Zhao, F., Li, W., Zhang, J., Liu, J., 2024. Influence of biotite content on the mechanical response of granite using a novel three-dimensional grain-based model and force chain analysis. ACS Omega 9 (8), 9603–9614. https://doi.org/10.1021/acsomega.3c09304.

Ghazvinian, E., Diederichs, M.S., Quey, R., 2014. 3D random Voronoi grain-based models for simulation of brittle rock damage and fabric-guided micro-fracturing. J. Rock Mech. Geotech. Eng. 6 (6), 506–521. https://doi.org/10.1016/j.jrmge.2014.09.001.

Guo, P., Bu, M., Zhang, P., Wang, J., Luan, Z., He, M., 2023a. Mechanical properties and crack propagation behavior of granite after high temperature treatment based on a thermo-mechanical grain-based model. Rock Mech. Rock Eng. 56 (9), 6411–6435.

Guo, P., Zhang, P., Bu, M., Wang, J., Zheng, X., He, M., 2023b. Microcracking behavior and damage mechanism of granite subjected to high temperature based on CT-GBM numerical simulation. Comput. Geotech. 159, 105385.

Hoek, E., Brown, E.T., 1997. Practical estimates of rock mass strength. Int. J. Rock Mech. Min. Sci. 34 (8), 1165–1186. https://doi.org/10.1016/S1365-1609(97)80069-X.

Hofmann, H., Babadagli, T., Yoon, J.S., et al., 2015a. A grain-based modeling study of mineralogical factors affecting strength, elastic behavior and micro-fracture development during compression tests in granites. Eng. Fract. Mech. 147, 261–275.

Hofmann, H., Babadagli, T., Zimmermann, G., 2015b. A grain-based modeling study of fracture branching during compression tests in granites. Int. J. Rock Mech. Min. Sci. 77, 152–162. https://doi.org/10.1016/j.ijrmms.2015.04.008.

Hu, X., Liao, D., Hu, H., Xie, S., Xie, N., Gong, X., 2024. The influence of mechanical heterogeneity of grain boundary on mechanical and microcracking behavior of granite under Mode I loading using a grain-based model. Rock Mech. Rock Eng. 57 (5), 3139–3169. https://doi.org/10.1007/s00603-023-03752-y.

Hu, X., Shentu, J., Xie, N., Huang, Y., Lei, G., Hu, H., Guo, P., Gong, X., 2023. Predicting triaxial compressive strength of high-temperature treated rock using machine learning techniques. J. Rock Mech. Geotech. Eng. 15 (8), 2072–2082. https://doi.org/10.1016/j.jrmge.2022.10.014.

Huang, L., He, R., Yang, Z., Tan, P., Chen, W., Li, X., et al., 2023. Exploring hydraulic fracture behavior in glutenite formation with strong heterogeneity and variable lithology based on DEM simulation. Eng. Fract. Mech. 278, 109020. https://doi.org/10.1016/j.engfracmech.2022.109020.
Jing, L., 2003. A review of techniques, advances and outstanding issues in numerical modelling for rock mechanics and rock engineering. Int. J. Rock Mech. Min. Sci. 40 (3), 283–353.
Kong, L., Shang, J., Ranjith, P.G., Li, B.Q., Song, Y., Cai, W., et al., 2024. Grain-based DEM modelling of mechanical and coupled hydro-mechanical behaviour of crystalline rocks. Eng. Geol. 339, 107649.
Kumari, W.G.P., Ranjith, P.G., 2019. Sustainable development of enhanced geothermal systems based on geotechnical research – A review. Earth Sci. Rev. 199, 102955.
Lan, H., Martin, C.D., Hu, B., 2010. Effect of heterogeneity of brittle rock on micromechanical extensile behavior during compression loading. J. Geophys. Res. 115 (B1). https://doi.org/10.1029/2009JB006496.
Li, M., Wu, J., Li, J., Zhuang, L., Wang, S., Zhang, F., 2022. Modeling of hydraulic fracturing in polymineralic rock with a grain-based DEM coupled with a pore network model. Eng. Fract. Mech. 275, 108801.
Li, X.F., Zhang, Q.B., Li, H.B., et al., 2018. Grain-based discrete element method (GB-DEM) modelling of multi-scale fracturing in rocks under dynamic loading. Rock Mech. Rock Eng. 51 (12), 3785–3817.
Liu, G., Sun, W., Lowinger, S.M., Zhang, Z., Huang, M., Peng, J., 2019. Coupled flow network and discrete element modeling of injection-induced crack propagation and coalescence in brittle rock. Acta Geotech. 14 (3), 843–868. https://doi.org/10.1007/s11440-018-0682-1.
Mahabadi, O.K., Tatone, B.S.A., Grasselli, G., 2014. Influence of microscale heterogeneity and microstructure on the tensile behavior of crystalline rocks. J. Geophys. Res. Solid Earth 119 (7), 5324–5341. https://doi.org/10.1002/2014JB011064.
Peng, J., Wong, L.N.Y., Teh, C.I., 2017. Influence of grain size heterogeneity on strength and microcracking behavior of crystalline rocks. J. Geophys. Res. Solid Earth 122 (2), 1054–1073. https://doi.org/10.1002/2016JB013469.
Peng, J., Wong, L.N.Y., Teh, C.I., 2021. Influence of grain size on strength of polymineralic crystalline rock: new insights from DEM grain-based modeling. J. Rock Mech. Geotech. Eng. 13 (4), 755–766. https://doi.org/10.1016/j.jrmge.2021.01.011.
Potyondy, D.O., 2010. A grain-based model for rock: approaching the true microstructure. In: Proceedings of Rock Mechanics in the Nordic Countries, pp. 9–12.
Potyondy, D.O., 2012. A flat-jointed bonded-particle material for hard rock. In: 46th U.S. Rock Mechanics/Geomechanics Symposium, pp. 2012–2501.
Potyondy, D.O., Cundall, P.A., 2004. A bonded-particle model for rock. Int. J. Rock Mech. Min. Sci. 41 (8), 1329–1364. https://doi.org/10.1016/j.ijrmms.2004.09.011.
Saadat, M., Taheri, A., 2020. Modelling micro-cracking behaviour of granite during direct tensile test using cohesive GBM approach. Eng. Fract. Mech. 239, 107297. https://doi.org/10.1016/j.engfracmech.2020.107297.
Sufian, A., Russell, A.R., 2013. Microstructural pore changes and energy dissipation in Gosford sandstone during pre-failure loading using X-ray CT. Int. J. Rock Mech. Min. Sci. 57, 119–131.
Ulusay, R., Türeli, K., Ider, M.H., 1994. Prediction of engineering properties of a selected litharenite sandstone from its petrographic characteristics using correlation and multivariate statistical techniques. Eng. Geol. 38 (1–2), 135–157.
Wang, S., Elsworth, D., Zhang, L., Zhao, X., Wang, T., 2024a. Hydro-grain-texture modeling of systematics of propagation, branching, and coalescence of fluid-driven fractures. Rock Mech. Rock Eng. https://doi.org/10.1007/s00603-024-04165-1.
Wang, S., Potyondy, D.O., Chu, W., Zhang, L., Zhao, X., Wang, T., 2024b. Investigation of meso-mechanical properties of Jinping dolomitic marble based on flat-joint model. J. Rock Mech. Geotech. Eng. In press.
Wang, S., Yasuhara, H., Zhuang, L., Zhao, X., Zhang, L., Wang, T., 2025. A novel hydro-grain-texture model to unveil the impact of mineral grain anisotropy on fluid-driven cracking processes in crystalline rock. Int. J. Numer. Anal. Met. 49 (2), 555–574.
Wang, S., Zhou, J., Zhang, L., Nagel, T., Han, Z., Kong, Y., 2023. Modeling injection-induced fracture propagation in crystalline rocks by a fluid–solid coupling grain-based model. Rock Mech. Rock Eng. https://doi.org/10.1007/s00603-023-03374-4.
Wang, T., Hu, W., Elsworth, D., et al., 2017. The effect of natural fractures on hydraulic fracturing propagation in coal seams. J. Pet. Sci. Eng. 150, 180–190.
Wang, T., Zhou, W., Chen, J., Xiao, X., Li, Y., Zhao, X., 2014. Simulation of hydraulic fracturing using particle flow method and application in a coal mine. Int. J. Coal Geol. 121, 1–13.
Yang, C., Xiong, Y., Wang, J., et al., 2020. Mechanical characterization of shale matrix minerals using phase-positioned nanoindentation and nano-dynamic mechanical analysis. Int. J. Coal Geol. 229.
Zhao, X., Elsworth, D., He, Y., Hu, W., Wang, T., 2021. A grain texture model to investigate effects of grain shape and orientation on macro-mechanical behavior of crystalline rock. Int. J. Rock Mech. Min. Sci. 148, 104971.
Zhou, J., Lan, H.X., Zhang, L.Q., et al., 2019. Novel grain-based model for simulation of brittle failure of Alxa porphyritic granite. Eng. Geol. 251, 100–114.
Zhou, J., Zhang, L., Yang, D., Braun, A., Han, Z., 2017. Investigation of the quasi-brittle failure of Alashan granite viewed from laboratory experiments and grain-based discrete element modeling. Materials 10 (7), 835.
Zhou, Y., Lv, W., Li, B., Liang, Q., 2024. Impact of soft minerals on crack propagation in crystalline rocks under uniaxial compression: a grain-based numerical investigation. Int. J. Numer. Anal. Meth. Geomech. 48 (8), 2020–2042. https://doi.org/10.1002/nag.3718.
Zhou, Y., Lv, W., Li, B., Liang, Q., Wang, S., 2025. A realistic 3D grain-based modeling approach for reproducing the mechanical and failure behavior of brittle granites. Int. J. Rock Mech. Min. 185, 105981.
Zhang, H., Sun, W., Xie, Q., Chen, Y., Tu, Z., Ban, Y., 2024. Study on mechanical properties and damage characteristics of acid corrosion in granite based on NMR technology. Eng. Geol. 340, 107678.
Zhuang, L., Jung, S.G., Diaz, M., Kim, K.Y., Hofmann, H., Min, K., et al., 2020. Laboratory true triaxial hydraulic fracturing of granite under six fluid injection schemes and grain-scale fracture observations. Rock Mech. Rock Eng. 53 (10), 4329–4344. https://doi.org/10.1007/s00603-020-02170-8.
Zhuang, L., Kim, K.Y., Jung, S.G., Diaz, M., Min, K., 2019. Effect of water infiltration, injection rate and anisotropy on hydraulic fracturing behavior of granite. Rock Mech. Rock Eng. 52 (2), 575–589.
Zhuang, L., Zang, A., 2021. Laboratory hydraulic fracturing experiments on crystalline rock for geothermal purposes. Earth Sci. Rev. 216, 103580.
Zhuang, L., Zang, A., Jung, S., 2022. Grain-scale analysis of fracture paths from high-cycle hydraulic fatigue experiments in granites and sandstone. Int. J. Rock Mech. Min. Sci. 157, 105177.